2016

# Early Assessment of Burn Severity in Human Tissue with Multi-Wavelength Spatial Frequency Domain Imaging

Chien Sing Poon
*Wright State University*

# EARLY ASSESSMENT OF BURN SEVERITY IN HUMAN TISSUE WITH MULTI-WAVELENGTH SPATIAL FREQUENCY DOMAIN IMAGING

A thesis submitted in partial fulfillment of the
requirements for the degree of
Master of Science in Biomedical Engineering

By

CHIEN SING POON
B.S., State University of New York at Buffalo, 2015

2016
Wright State University

WRIGHT STATE UNIVERSITY

GRADUATE SCHOOL

October 10, 2016

I HEREBY RECOMMEND THAT THE THESIS PREPARED UNDER MY SUPERVISION BY Chien Sing Poon ENTITLED Early Assessment of Burn Severity in Human Tissue with Multi-Wavelength Spatial Frequency Domain Imaging BE ACCEPTED IN PARTIAL FULFILLMENT OF THE REQUIREMENTS FOR THE DEGREE OF Master of Science in Biomedical Engineering.

_____

Ulas Sunar, PhD.
Thesis Director

_____

Jaime E. Ramirez-Vick, Ph.D.,
Chair, Department of Biomedical, Industrial and Human Factors Engineering

Committee on
Final Examination

_____

Ping He, Ph.D

_____

Jeffrey B. Travers, M.D., Ph.D.

_____

Ulas Sunar, Ph.D.

_____

Robert E.W. Fyffe, Ph.D.
Vice President for Research and
Dean of the Graduate School

# Abstract

Poon, Chien Sing. M.S.B.M.E. Department of Biomedical, Industrial and Human Factors Engineering, Wright State University, 2016. Early Assessment of Burn Severity in Human Tissue with Multi-Wavelength Spatial Frequency Domain Imaging.

Burn injuries such as thermal burns, which are caused by contact with flames, hot liquids, hot surfaces, and other sources of high heat as well as chemical burns and electrical burns, affects at least 500,000 people in the United States, to which 45,000 of them require medical treatment and 3,500 of them result in death. It has also been reported that in the United States alone, fire results in a death approximately every three hours and an injury every 33 minutes. Early knowledge about burn severity can lead to improved outcome for patients. In this study, the changes in optical properties in human skin following thermal burn injuries were investigated. Human skin removed during body contouring procedures was burned for either 10 or 60 seconds using a metal block placed in boiling water. Multi-wavelength spatial frequency domain imaging (SFDI) measurements were performed on each sample and the optical properties (absorption and scattering parameters) were obtained at each wavelength. Multi-wavelength fitting was used to quantify scattering parameters, and these parameters were compared to histologic assessments of burn severity. Our results indicate substantial changes in optical parameters and changes, which correlate well with respect to burn severity. This study shows the characterization of thermal burn injury on human skin *ex vivo* by using the

optical method of SFDI with high sensitivity and specificity. Due to more challenging conditions of layered skin structures with differing thickness in humans, ongoing work tackles combining high-resolution ultrasound imaging with SFDI for more accurate quantification of optical properties during *in vivo* clinical studies.

# Table of Contents

# List of Figures

# List of Tables

# Acknowledgements

I would like to take this opportunity to thank my advisor, Dr. Ulas Sunar, to whom I am indebted. He introduced me to the world of optical imaging and gave me the opportunity to work for him. His strategic, practical, and focused approach has always challenged me to stay on track and to think in a broader way, providing me with an education that goes beyond the traditional classroom. I would also like to thank Dr. Ping He and Dr. Jeffrey Travers for being part of my committee. Dr. Ping He, with his experience and meticulous nature, has challenged me to strive for excellence in every detail of my work with no room for compromising, an uncommon quality that I truly appreciate. Dr. Jeffrey Travers always adds a little fun to the people around him, especially for his patients for whom he is constantly thinking how to improve their quality of life. I also want to thank the people in the lab: Daniel Rohrbach, who has helped me throughout my thesis preparation and is a great resource; Jeremy Kress, who contributed to the instrumentation; Jun Li, who gave important suggestions; and other lab members such as Aaron Madaris, Syed Zaidi and Zahra Meghjani who are just enjoyable to talk to and work with.

I also want to thank my friends and family for their support. I especially thank my parents who had the foresight to plan for my education and gave me the liberty to choose what I wanted for myself. Finally, I would like to thank Immanuel, a friend and mentor like no other. He constantly pointed me in the right direction despite my rebellion. Ultimately, to Him I owe it all.

# CHAPTER 1: INTRODUCTION

## 1.1 Introduction

Burns are a common type of injury among people. They can occur anywhere from a household setting where heat, electricity and friction might be the source of injury to industrial settings where radiation and chemical agents might be the main source of injury [1], [2]. Each year in the United States, at least 500,000 people are affected by burn injuries [3], to which 45,000 of them require medical treatment and 3,500 of them result in death. It has also been reported that approximately every three hour, someone died from fire and every 33 minutes someone was injured by fire in the United States [4].

These injuries are often categorized by different grades ranging from I through IV, with grade II subdivided into IIA and IIB. They are also described as superficial epidermal, superficial partial, deep partial, full-thickness, or deep burn [1], [2], [5]–[7]. These grades define the layers of skin, which are damaged by the burn, so that the depth of the wound can be approximated. In a grade I burn, only the epidermis – upper most layer – is damaged. These burns are usually non-critical as they typically heal on their own within a week. In a Grade II burn, the dermis is usually damaged. The extent of damage within the dermis dictates the appearance (blistering and scarring of the wound), sensitivity to pain and time needed for healing. The most severe burns, grades III and IV, damage the skin down to the hypodermis so the skin does not heal spontaneously and thus requires debridement and skin grafts [1], [2], [5], [8].

Clinicians can easily diagnose grades I, III and IV burns due to their distinct physical features. However, the challenge is with accurately classifying a burn between grade IIA and grade IIB [1], [2], [9]. The wound care procedure is different between both of these, with the former requiring less treatment and the latter requiring specialized care with the possibility of skin grafts. Therefore, it is important to know the depth of burn to determine the appropriate treatment.

## 1.2 Motivation

Currently, the "gold standard" in burn severity evaluation is through punch biopsies with subsequent histological analysis [2], [9]. This method is carried out on a small excised portion of the wound, which is cryo-sectioned and stained with hematoxylin and eosin [7]. With this method, the structural changes due to the burn can be visually inspected on the cellular level by investigating the depth of necrosis to which the burn depth can be accurately quantified [2], [7], [9]. However, the major drawback in this approach is that it is invasive and that it is a point measurement at a fixed time point to which the depth of burn are usually non-homogenous and can progress over time.

There are several other approaches in evaluating burn severity. The most widely used of these approaches is a subjective evaluation of the external features present in the wound [1], [2], [9]. These include appearance, capillary refill, and burn wound sensitivity to touch and pinprick [2]. However, these methods are unreliable and highly dependent on the experience of the clinicians. To overcome this problem, clinicians have tried taking images of the affected and evaluating it with the burn team to get a majority

opinion [2]. This approach reduces the bias, but it still suffers from accurately determining the burn severity, and it also removes the tactile and stereo component as part of the evaluation due to the two-dimensional nature of the images.

These problems present the need for an approach where the severity and depth of burn can be accurately quantified non-invasively. This approach should have enough contrast to differentiate between different grades of burn as well as being quick and efficient.

Spatial Frequency Domain Imaging (SFDI) is a wide field imaging technique that projects sine wave patterns of light on the sample [10], [11]. The pattern of the projected light is modulated at increasing spatial frequency with three different phases using a Digital Micro-mirror Device (DMD) and each pattern is acquired with a camera. These images are then demodulated to obtain the diffuse reflectance. From the reflectance images, the optical properties (absorption and scattering) can be quantified at each pixel creating a quantitative two-dimensional map. Since each pixel is treated as a single point of observation, hundreds of thousands of points can be simultaneously obtained, which is otherwise unfeasible in many other point-based approach. This is especially important for burns, which may vary in severity across their extent making point measurements unfeasible [2], [12], [13]. Multi-wavelength SFDI allows for the quantification of functional, blood-related parameters such as tissue deoxy-, oxy-, total-hemoglobin concentrations, and oxygen saturation [12]–[16] as well as structural, tissue scattering parameters related to the number and size of “scatterers” [17]–[20].

## 1.3 Goals

We hypothesize that the properties and structure of the skin changes when burned. Quantitative information of absorption and scattering can be indicative of burn severity and depth [12]–[14]. Therefore, there is a need to obtain multiple tissue parameters, non-invasively. Towards this goal, we built a SFDI system and verified its ability in quantifying the optical properties of the target. We also performed a study on excised tissues with varying burn severity and correlated the results to the histological results to deduce a simple model for assessing the burn severity using SFDI.

## 1.4 Thesis Outline

In this thesis, I will quantify optical absorption ($\mu_a$) and reduced scattering ($\mu_s'$) by using SFDI on excised human tissue, which has been burned for different lengths of time to simulate different burn grades.

Chapter 2 presents the background information on the physiology of the human skin, the different grades of burn and the methods that are used in the evaluation of burn severity. The background information for optical parameters such as absorption, scattering and photon diffusion in tissues will also be covered.

Chapter 3 presents the background for optical properties in human tissue as well as the theory underlining SFDI. It will also cover the method used in quantifying the optical properties as well as the determination of hemoglobin parameters from the diffuse reflectance images. The instrumentation and validation of the SFDI system will also be covered.

Chapter 4 presents a study obtained from an *ex vivo* burnt skin using SFDI. The methods and results of this study will be discussed in this chapter.

Chapter 5 will cover the future directions in relation to the current work. Particularly, using a two-layer model to reduce the error in approximating the optical and function parameters of the skin and using depth information from high-frequency ultrasound to reduce the uncertainty in the curve fits.

# CHAPTER 2: BACKGROUND

## 2.1 Introduction

The skin is the largest organ in humans. It serves many purposes such as regulating body temperature, acting as a barrier to protect internal organs and permitting interaction with the external environment by different sensation [21], [22]. There are also different skin components that provide various functionalities depending on the location on the skin [21], [22]. Components such as the sweat glands and the sebaceous glands vary in concentration or may be absent from certain locations on the human skin.

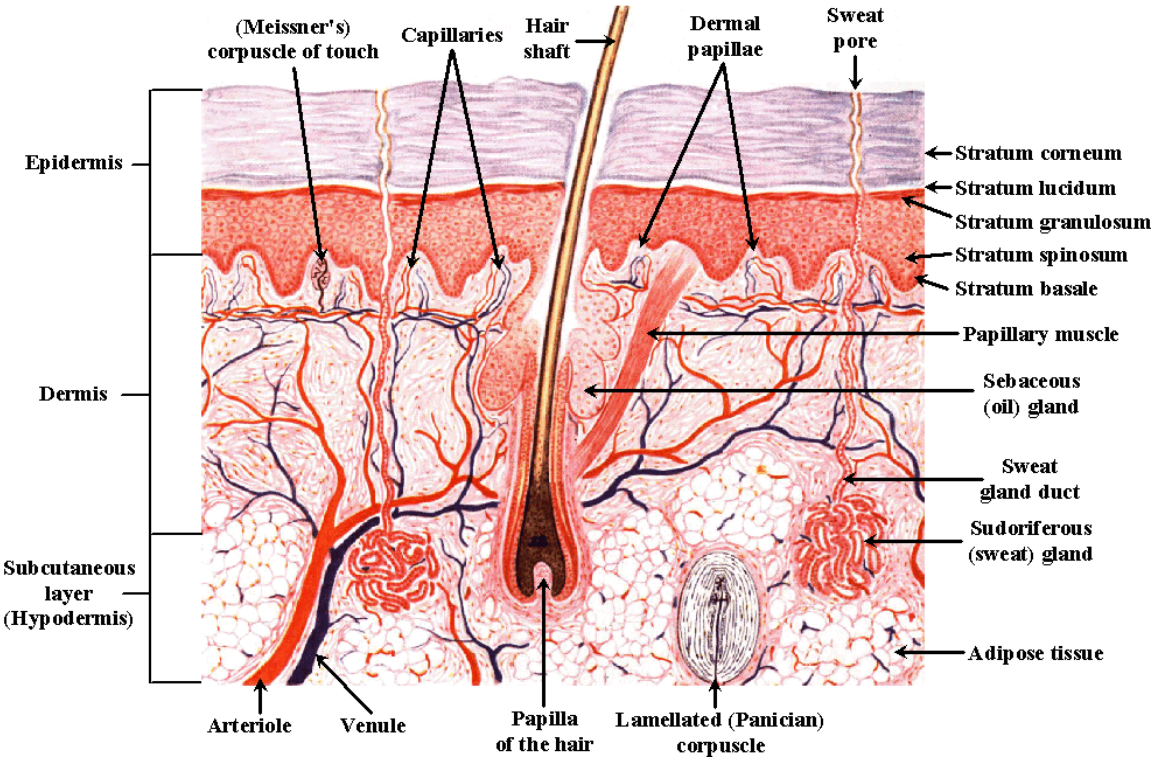


Figure 2.1. Different layers of the human skin. Retrieved from [23].

The human skin has three primary layers: epidermis, dermis and hypodermis. The epidermis is the outermost layer of the skin. Its primary purpose is being a protective barrier to prevent pathogens, microbes and other external elements from entering the body [21], [22]. It also acts as a conductor to regulate body temperature in humans. The dermis contains most of the functional components of the skin, such as the nerve endings, which provide the sense of touch as well as blood vessels, which nourish and remove waste from the surrounding cells. The hypodermis is primarily made up of fat. It cushions and insulates the internal organs from external environmental stresses.

### 2.1.1 Epidermis

The epidermis is primarily made up of keratinocytes that produces a fibrous structure protein known as keratin [22]. The strength and elasticity of the human skin is produced by keratinization, which is the assembling of keratin monomers into larger bundles known as the intermediate filaments [24]. This process is responsible for α-keratin that assembles into the human hair, the outermost layer of the epidermis and nails.

Main components of the epidermis is the *Stratum Corneum,* and the *Stratum Basale* (Figure 2.2), some of which may only be present in the skin at certain locations of the human body [22]. At the basal layer of the epidermis, the *Stratum Basale* is a layer only a few cells thick consisting of basal keratinocyte stem cells. This layer is responsible for the constant differentiation of keratinocytes to replace the dead or dying superficial layers of the epidermis. When the *Stratum Basale* is compromised, as in an injury, scarring in the form of skin discoloration may be present.

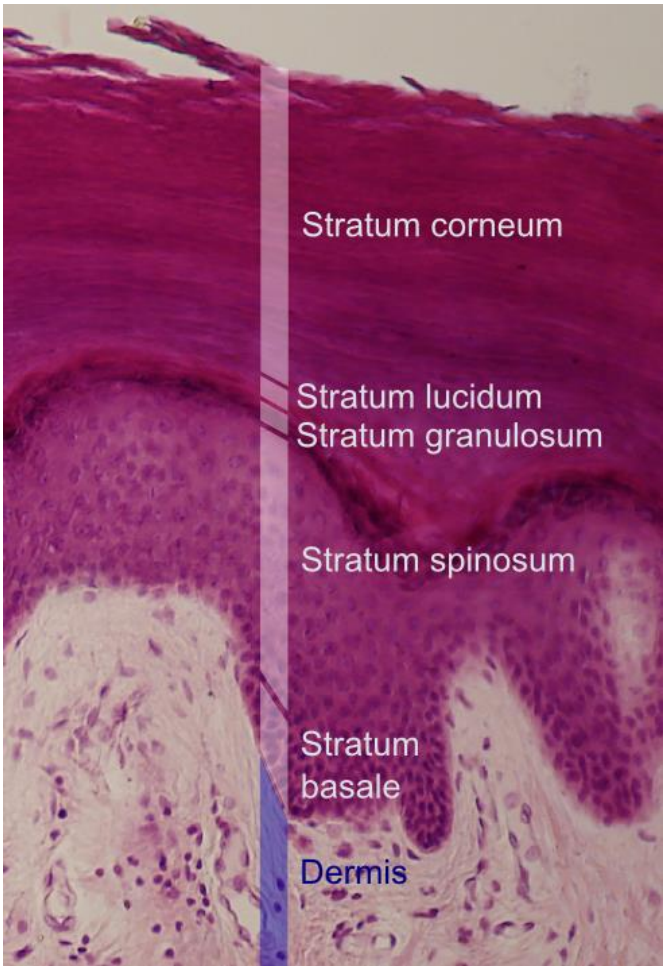


Figure 2.2. Layers of the epidermis. Retrieved from [25]

The *Stratum Lucidum* is a layer between *Stratum Granulosum* and *Stratum Corneum* that is only found in areas of thick skin such as the palms of the hand and the soles of the feet. Due to this additional layer, the epidermis is thicker and less susceptible to damage compared to other parts of the skin. The keratinocytes in the lower layers of the epidermis go through cornification to produce the *Stratum Corneum* which is also the main physical barrier of the skin [26].

### 2.1.2 Dermis

The dermis contains most of the nerve endings. This explains the increase in pain associated with deeper burns that reach this layer [1], [2], [5], [9]. The dermis is approximately one to three millimeters thick, and it contains many other cells that provide different functionalities [21], [27], [28]. Examples of such cells are the hair follicles, sweat glands, sebaceous glands, lymphatic vessels and blood vessels. The dermis also serves to cushion the internal organs from environmental stresses.

As indicated previously, one of the most important features in the dermis is the nerve endings. The nerve endings support the sensations felt by the skin when it interacts with the environment. When the nerve endings are exposed through a degradation of the epidermis, the sensitivity is greatly increased, therefore increasing the sensation of pain. Another important feature in the dermis is the blood vessels. Blood vessels in the form of capillaries are plentiful in the dermis, due to the need for providing nourishment and waste removal in the surrounding cells [22]. When a burn invades the dermis superficially, the inflammatory process leads to a pink appearance [29]. When the burn progresses deeper into the dermis, more of the blood vessels are exposed, leading to a "bloody" appearance [29].

### 2.1.3 Hypodermis

The hypodermis – also known as the subcutaneous fat layer – is the layer that connects the dermis to the muscles. It is mainly present to serve as insulation and padding to the internal organs, therefore it is usually much thicker relative to the first two layers

[30]. For burns that persist into the hypodermis, a pale appearance is usually seen as the fat is being exposed [29].

## 2.2 Burn Grades in Relation to Severity

Proteins begin to break down when heated to a temperature that is greater than 44°C [31]. This process causes the proteins to lose their three dimensional structure and chemical bonds, resulting in a change in outward appearance and texture of the skin. A common way used by clinicians to approximate the burn severity is by characterizing them in different grades. This grading system as shown in (Figure 2.3) is categorized by four roman numerals and has the following description: superficial, superficial partial thickness, superficial deep thickness, full thickness and deep burn [2], [9].

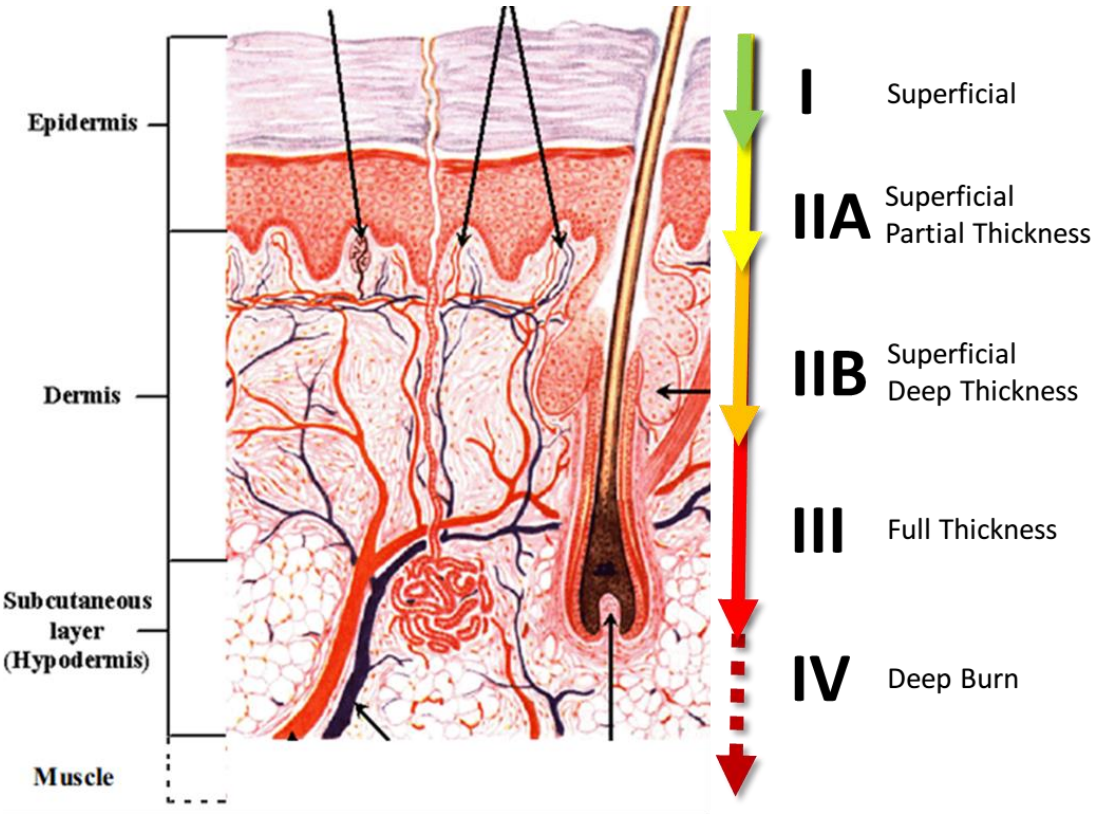


Figure 2.3. Different burn grades in relation to the layers of skin damaged. Adapted from [23].

## 2.2.1 Grade I Superficial Burn

In Grade I superficial burns, the burn persists only within the epidermis, which is approximately 100 microns deep [27], [28]. Burns of this grade are usually non-vital and can be caused by UV radiation from the sun, short duration to open sources of heat or minor flash injuries caused by small explosions. The superficial layers – usually *Stratum Corneum*– of the epidermis are burnt, which may cause an increase in regional blood flow, resulting in a "pinkish" appearance (Figure 2.4). The wound is usually painful to

touch, and can take up to seven days to heal [2], [9], [32]. Scarring usually does not occur in this grade.

Figure 2.4. Example of a Grade I burn on a human shin. Retrieved from [33]

## 2.2.2 Grade IIA Superficial Partial Thickness Burn

Grade II burns are the only category that is subdivided into further groups. It is also in this grade that clinicians have the most difficulty in approximating the burn severity. It is important, since the burn severity in this grade may determine if the patient should be referred to a specialist burn center for further care [2], [9].

These burns persist from the epidermis to the superficial layer of the dermis. These types of burns are very painful due to the exposure of sensory nerves. There is also increased blood flow in that area, which causes a “reddish” appearance [2], [9], [29]. Another differentiating factor from grade I burn is the presence of blisters. The burnt skin covering the blister is usually separated from the epidermis by inflammatory blister fluid (Figure 2.5).When the blister ruptures, the pink looking dermis beneath is exposed.

Usually, these burns will heal spontaneously by epithelialization within 14 days [2], [9], [32].

Figure 2.5. Example of a Grade IIA burn on a human forearm. Retrieved from [8]

### 2.2.3 Grade IIB Superficial Deep Thickness Burn

Grade IIB burns can extend from the middle of the dermis to the boundary close to the hypodermis, leaving minimal viable dermal tissue at the base. In this grade, the burn usually persists for a short period after the initial incident [5], [29]. To prevent burn wound progression, it is important to preserve the remaining viable tissue at the base layer [5]. Some or most of the nerve endings can be damaged, resulting in a severely decreased sensation of pain, which depends on the extent of damage to the nerve endings. Similarly, as some of the capillaries remain viable, blood flow is present and can vary from a delayed response to a sluggish response [2]. Blisters may or may not be present in this grade, and tend to be dry, with diminished blister fluid compared with burns that are more superficial (Figure 2.6). The time needed for healing may be unpredictable and it

usually requires regular review in order to determine appropriate treatment [2], [9], [32]. The underlying dermis may appear to be red due to the extravasation of blood cells [29].

Figure 2.6. Example of a Grade IIB burn on a human hand. Retrieved from [8].

### 2.2.4 Grade III Full Thickness Burn and Grade IV Deep Burn

Full thickness burns destroy the epidermis and the dermis and penetrates into the hypodermis. Due to the penetration into the hypodermis and the destruction of capillaries in the dermis, these burns have a white, waxy or even charred appearance (Figure 2.7) [29]. Intuitively, there is usually no sign of blood flow. Since most of the sensory nerves endings in the dermis are destroyed in a full thickness burn, there is usually minimal sensation to pain [29]. The cells responsible for regeneration are also destroyed, thus the healing process is usually lengthy. For a full thickness burn, a skin graft is typically required [2], [5], [9].

Figure 2.7. Example of a Grade III burn on the back of a human. Retrieved from [8]

Deep burns share many of the characteristics of full-thickness burns. However, for a grade IV deep burn, almost the whole layer of skin is destroyed, leaving the underlying structures such as the muscle or the bones exposed.

## 2.2.5 Summary of Burn Grades

Clinicians often categorize incoming burn patients by the penetration depth of the burn and the total body surface area affected by the burn. The penetration depth is categorized into different burn grades, as described above. Each of these grades has their own physical characteristics, which is summarized in (Table 2.1).

Table 2.1. Overview of different burn severity characteristics

| | Grade I | Grade IIA | Grade IIB | Grade III | Grade IV |
|---|---|---|---|---|---|
| **Pathology** | Epidermis only | Epidermis and upper dermal layers | Epidermis and most of the dermis | Upper layers to the hypodermis | All layers of the skin |
| **Appearance** | Dry and red | Pale and pink | Dark pink to "bloody" | White, waxy or charred | Charred, exposed muscle or bones |
| **Sensation** | Maybe painful | Usually very painful | Maybe painful | Decreased sensation | Minimal pain |
| **Circulation** | Normal to increased | Increased | Sluggish | No | No |
| **Color** | Red, warm | Pink | White/Pink/Red | White/Black | White/Black |
| **Blisters** | Minimal | Yes | Some | No | No |
| **Healing** | < 7days | 7 - 21 days | > 21 days | Does not heal spontaneously | Does not heal |
| **Scarring** | No scar | Discoloration | Likely to get hypertrophic scarring | Will scar | Will scar |

It is usually easy to determine the superficial burns (Grade I) as well as the deeper burns (Grades III and IV). However, there is an existing challenge in diagnosing the correct burn severity within the second grade [2], [5]. It is also within the second grade where clinicians decide if the patient should be referred to a specialist burn center for surgery. It is important to note that for most cases of burn injuries, the wound is non-homogenous. It can vary from a full thickness burn at the point of contact to the heat source – also known as the zone of coagulation – and spread outwards with decreasing burn severity and different characteristics as shown in the commonly used Jackson's burn model (Figure 2.8) [29].

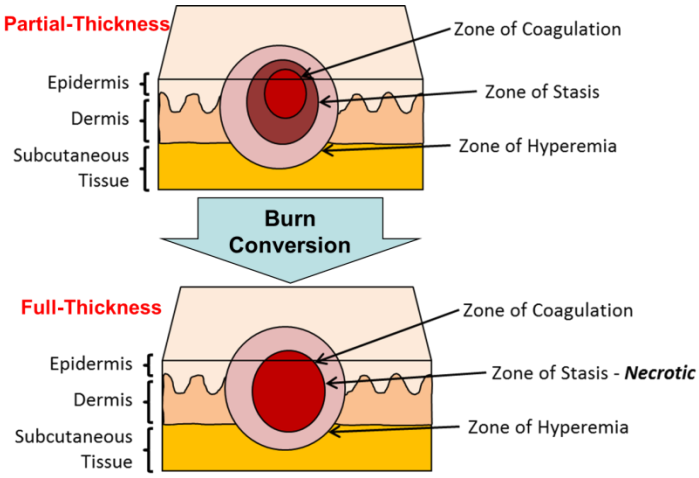


Figure 2.8. Schematic representation of Jackson's burn model. Burn injuries can evolve from superficial partial-thickness burns to a deeper burn through the necrosis of the zone of stasis.

## 2.3 Existing Methods for Burn Severity Approximation

Since a burn usually penetrates deeper within the first few hours, a quantitative method that can assess the burn severity accurately and efficiently is highly desirable [2], [29]. The method has to monitor the wound continuously or at short intervals. Moreover, the wound is usually heterogeneous and can cover a large portion of the skin. The wound may also be sensitive or fragile to touch [29]. With these requirements in mind, many existing methods in assessing burn severity are far from ideal [2], [9]. In the next section, the most widely used clinical methods in assessing the burn severity will be briefly discussed.

### 2.3.1 Clinical Evaluation

Clinical evaluation of the burn wound is the most widely used and the least expensive method of assessing burn severity [2], [9], [29]. This method is dependent on the subjective evaluation from the clinicians when evaluating external features of the wound such as appearance, capillary refill, and sensitivity to touch and pin prick [2], [29]. Among these methods, capillary refill is the most useful clinical method to assess burn severity [2]. In this particular method, clinicians observe the extent and speed of capillary refill (Figure 2.9), providing a quick approximation to evaluating the burn severity. However, none of the external features is sufficiently reliable, accurate or quantitative, achieving a combined correct severity assessment in only about two out of three cases [2], [9]. In most of the cases, severity overestimation contributes to the majority of these errors [2], leading to a waste of resources. This problem is further made crucial by intermediate grade II burns, where the external features may confound with each other as opposed to grade I and grade III burns which are more easily determined.

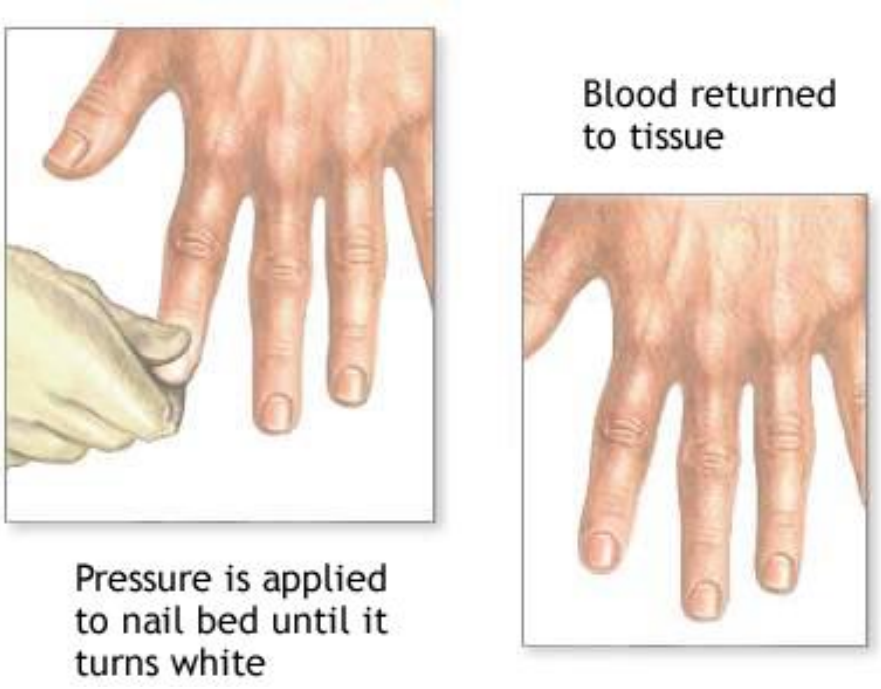


Figure 2.9. Procedure for testing capillary return. Retrieved from [15].

Since these methods are subject to the clinician's perception, there is considerable variation between burn severity assessments performed by different clinicians [34]. In the first few hours post burn, the burn is constantly evolving. This results in an increasing zone of stasis (Figure 2.8) and thereby increasing burn severity [29]. Studies have suggested that early intervention may slow the rate of burn evolution [5]. Therefore, an early and reliable burn severity assessment is of great importance, especially for the emergency department of local hospitals where most burn patients arrive.

## 2.3.2 Punch Biopsy

Currently, the “gold standard” for burn severity assessment, is taking a punch biopsy of burn tissue and analyzing it with histology [2], [7], [12], [13], [29]. Assessment is performed by extracting a small piece of tissue deep into the skin (Figure 2.10).

The dermatopathologist then takes thin sections of the tissue and stain it with hematoxylin and eosin [7], to which an accurate assessment of burn severity can be made by looking at the changes to cellular vitality and the denaturation caused by burns.

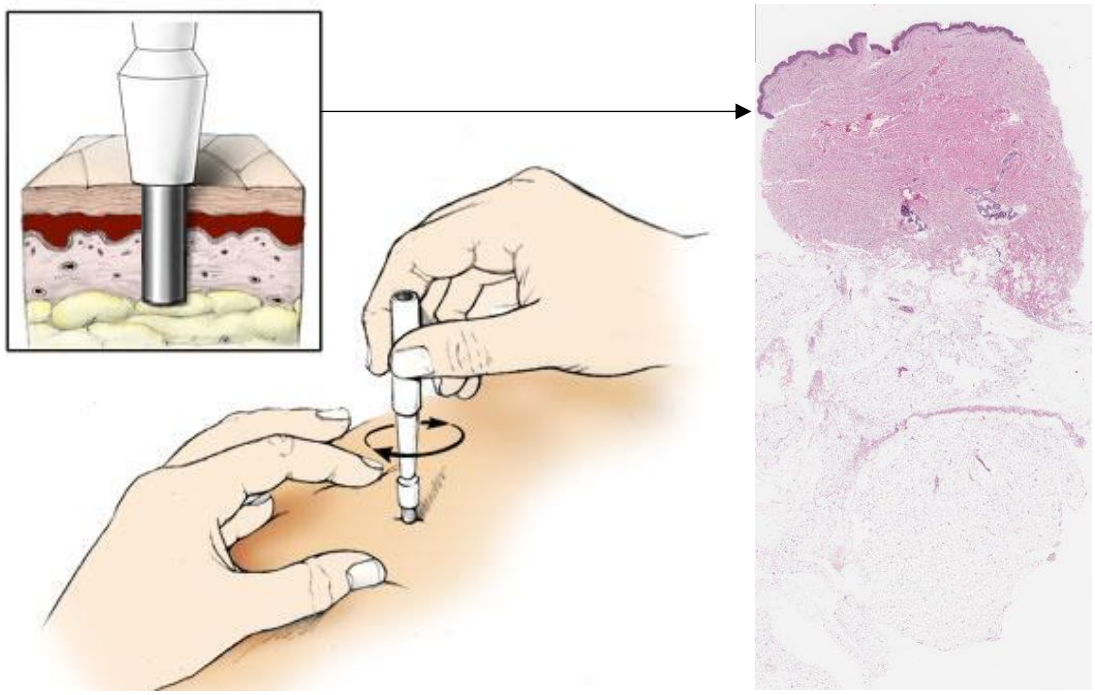

Figure 2.10. Procedures for taking a punch biopsy, which is sent for histopathology analysis. Adapted from [84].

Although biopsy with histological analysis is a quantitative and accurate measure of the burn severity, there are still multiple critical shortfalls. This method only samples the wound at a single point, which suffers from sampling error since a burn wound is

rarely homogenous [2]. Taking multiple samples in order to characterize the whole wound can be stressful and invasive to the patient. In addition, taking multiple points on the wound becomes impractical due to amount of resources needed to prepare each samples for analysis. Moreover, biopsies only provide a snap shot view of the wound at a single time point, neglecting the burn wound evolution [2], [12], [13]. Nevertheless, biopsies remain the primary tool in research to compare against new modalities [2], [12], [13], [29].

## 2.4 Skin Tissue Optical Properties

In medical optical imaging, light is being used as diagnostic tool. The main wavelength range is from visible (VIS) to near infrared (NIR) [~500nm – 900nm]. As photons enter the skin, they can be either absorbed (Figure 2.11a) or scattered (Figure 2.11b) and for thick tissue photons undergo both [35]–[38]. By quantifying these physical parameters, several other physiological parameters can be obtained. In addition, when the measurements are acquired at multiple time points it is possible to quantify the changes in these parameters, which may provide feedback on burn progression over time. These parameters will be briefly discussed in the following sections.

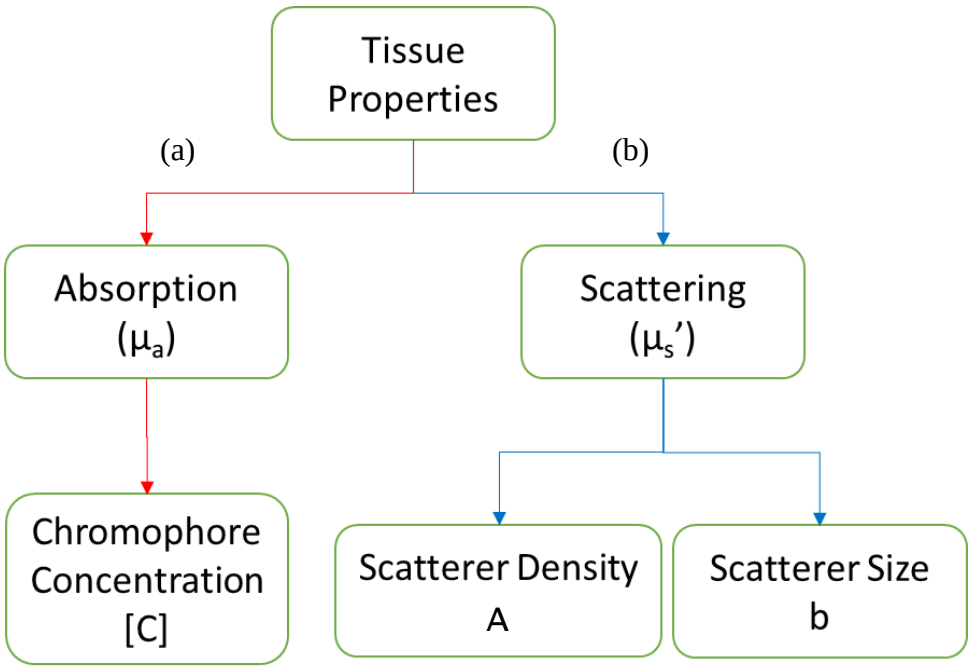


Figure 2.11. Optical properties of the tissue. (a) Absorption, $\mu_a$, is linearly dependent on the sum of chromophore concentration, C. (b) Scattering, $\mu_s'$, is dependent on both the density, A, and the size of the "scatterer", b.

## 2.4.1 Absorption in Skin Tissue

Absorption happens when the energy of the photons is lost to the surrounding medium [37], [39]. The rate of this energy loss is related to the absorption coefficient, $\mu_a$, of the medium. Since the unit for $\mu_a$ is the inverse of distance (typically $mm^{-1}$ or $cm^{-1}$) the absorption coefficient represents the distance most photons travel before being absorbed. This absorption of energy is linearly related to the sum of the concentration, C, and the molar extinction coefficient, $\varepsilon$, of the tissue chromophores (Figure 2.12) [14]–[16], [40].

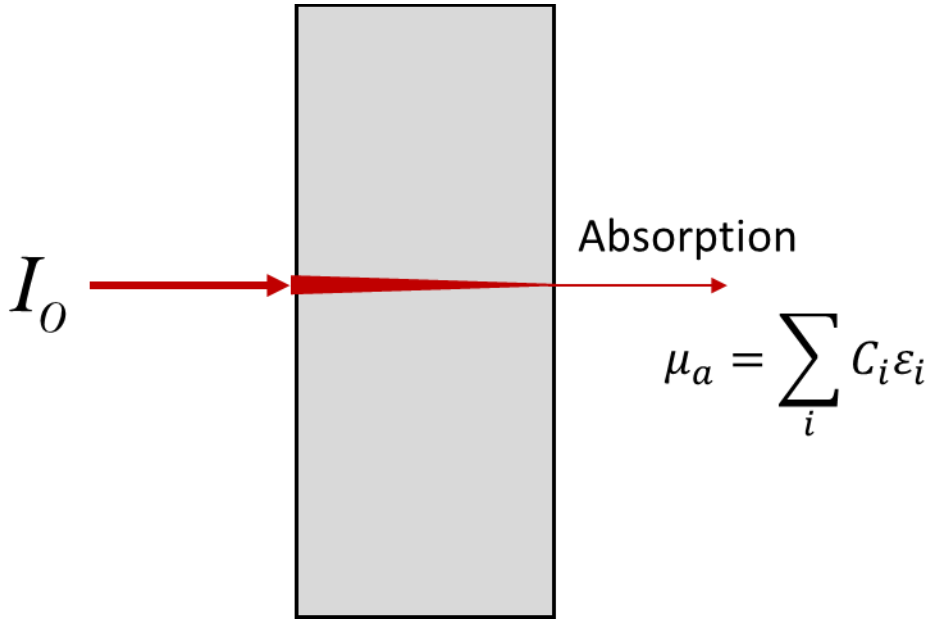


Figure 2.12. Absorption of light is linearly dependent on the sum of the concentration, C, multiplied by the absorption coefficient, ε, of the chromophore.

In skin, some of the most important chromophores are hemoglobin, melanin and water [41]–[43]. Each of these chromophores is characterized by their absorption coefficient as a function of wavelength (Figure 2.13). In particular, hemoglobin, which is the functional component in blood, can exist in two states: oxygenated and deoxygenated [14]–[16], [40]. These two states have distinctively different absorption coefficients at each wavelength (Figure 2.13), which could be used to separate them.

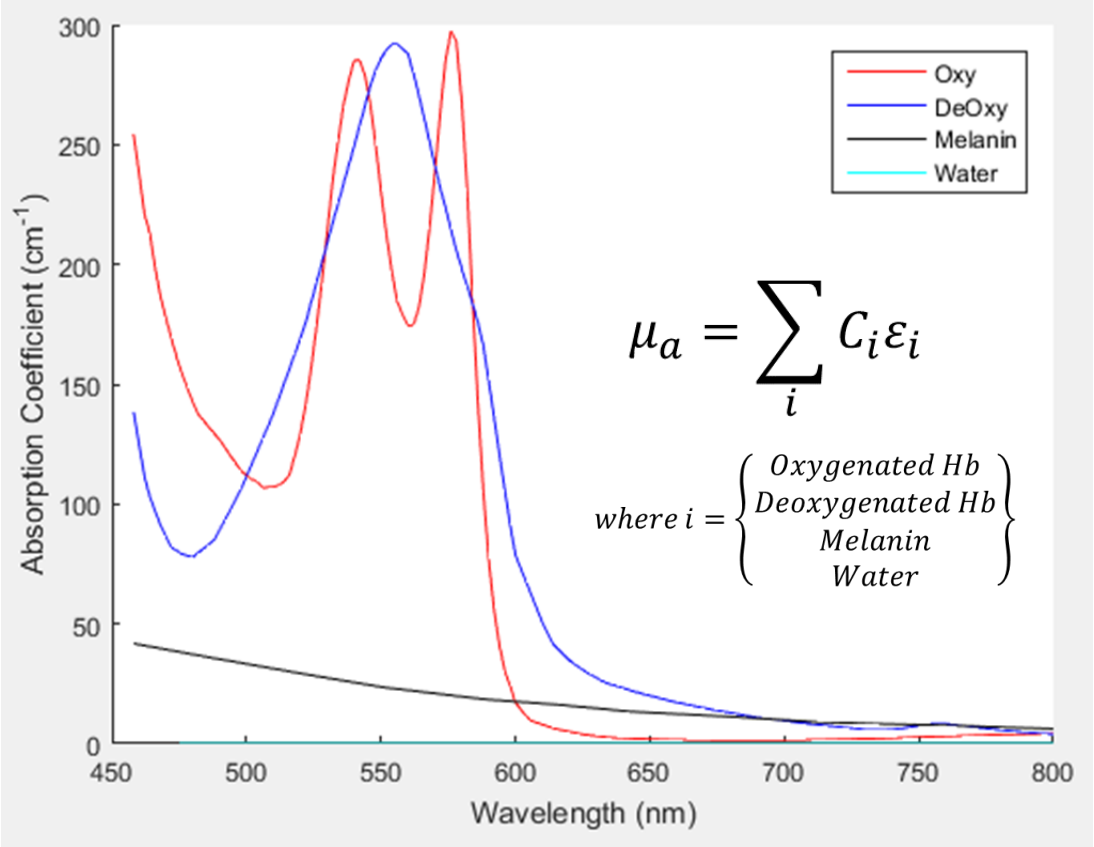


Figure 2.13. Absorption coefficient spectra of oxygenated, deoxygenated, melanin and water. The absorption parameter of the skin can be approximated by the combination of these biologically significant chromophores.

Since, blood is often a good indicator of various lesions such as burn wounds, investigating the oxygen saturation of blood and the total hemoglobin concentration can provide functional contrast to the state of the wound [14]–[16], [40]–[43].

## 2.4.2 Scattering in Skin Tissue

Photons in tissue can change their direction of travel and phase – also known as being "scattered" – as they encounter a turbid media such as the skin (Figure 2.14). Tissue is a scattering dominant medium, which means optical scattering is much higher than absorption. For example, while skin optical absorption parameter at ~600nm is approximately 0.1mm$^{-1}$, scattering parameter ($\mu_s$) is 10mm$^{-1}$, indicating a ~100-fold differences between these parameters. This numbers indicate that on average an absorption phenomenon occurs every 10mm, while a photon scatters and change direction in skin tissue every 100 microns. Thus, low energy-photon in VIS and NIR range propagates in skin with "zig-zag" paths (Figure 2.14), rather than straight paths, as it would be for the case of high-energy photons in x-ray beams.

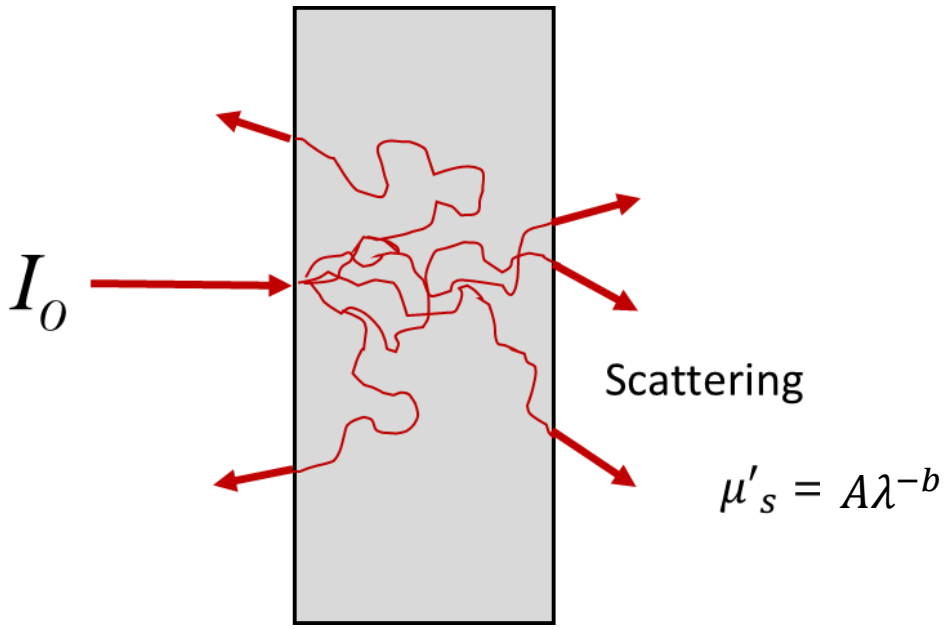


Figure 2.14. Scattering causes photons to change directions in a turbid media such as the skin.

The scattering phenomena in tissue can be described by Rayleigh and Mie scattering (the power law). It has been shown that for most cellular tissues – such as skin – the scattering phenomena can be sufficiently approximated without Rayleigh scattering [44]. Mie scattering occurs when photons collide with particles that are close to or larger than the wavelength of the incident light (Figure 2.15) [17], [45]. This results in most of the light travelling in the same direction of the incident light, which is known as forward scattering. It has been shown that tissue scattering can be represented as a power law, $A\lambda^{-b}$, where A is the density and b is the size of the "scatterer" (Figure 2.11b) [17], [45]. As the number of "scatterers" in an area increases, the scattering parameter, A, will also increase. This phenomenon is reversed for scattering parameter, b, where the increase in the particle size decreases b [17]. When b = 4, Rayleigh scattering ($\lambda^{-4}$) dominates when the particle is much smaller than the incident wavelength. The skin tissue was investigated by Jacques, and he showed that b = 0.838 for the epidermis and the dermis of the skin [17], [46].

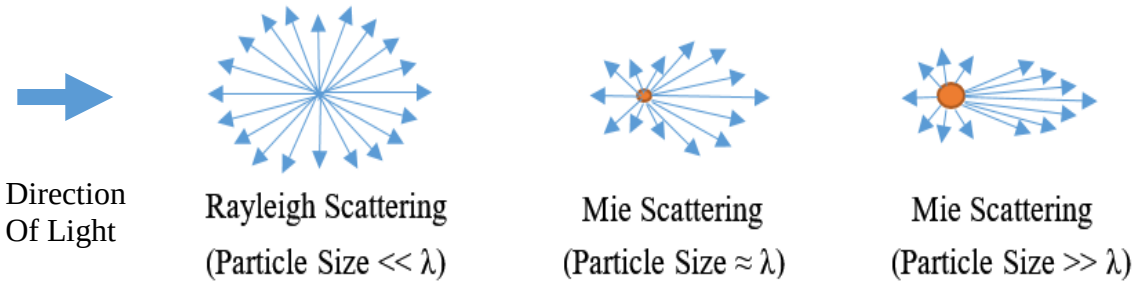


Figure 2.15. Mie scattering dominates when the particle size is close to or larger than the wavelength of the incident light, resulting in forward scattering. When the particle size is smaller than the wavelength of light, Rayleigh scattering dominates.

### 2.4.3 Photon Diffusion in Skin Tissue

Photons propagating in a turbid medium such as the skin can be described with the transport equation and approximated with the diffusion equation to arrive at the following classical equation [47]–[50]:

$$\frac{\partial \varphi(\boldsymbol{r},t)}{\partial t} = D\nabla^2\varphi(\boldsymbol{r},t) - v\mu_a\varphi(\boldsymbol{r},t) + vS_0(\boldsymbol{r},t) \tag{2.1}$$

where $S$ is the isotropic source term, $D = v / 3\mu_s'$ is the diffusion coefficient, $v$ is the speed of light in the medium, $\varphi(\boldsymbol{r}, t)$ is the photon density as a function of distance and time. In this equation, the first term on the right hand side represents the scattering of photons, the second term represents the photon density losses due to absorption and the last term represents the source of photon density.

This phenomenon – diffusion theory – will serve as the model for extracting the absorption and scattering parameters from the diffuse reflectance. This will be explained further in the next chapter.

#### 2.4.3.1 Diffuse Reflectance in Skin Tissues

Since light does not penetrate whole body, the primary way of measuring tissue like skin by optical imaging is through the reflection of light from tissue. There are two types of reflection. When the medium is smooth, specular reflection occurs (Figure 2.16a), when it is rough, diffuse reflection occurs (Figure 2.16b) [48], [51]. In most optical imaging cases, specular reflection is a source of noise as it readily reflects off the

surface of the medium, only carrying surface information with it. Specular reflection can be easily removed by cross polarizing the incident and the reflected light [15], [16].

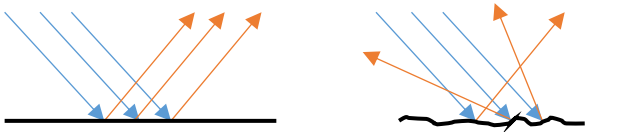

a. Specular Reflection b. Diffuse Reflection

Figure 2.16. Two types of reflection. (a) When light interacts with a smooth surface, specular reflection occurs. (b) When light interacts with a rough surface, the light is scattered in many directions, which is also known as diffuse reflection.

In biomedical optical imaging, the light that has interacted within the sample though multiple absorption and scattering events and reflected out contains the most information of interest. This type of reflection is known as diffuse reflection (Figure 2.17) [42], [52]–[54]. Diffuse reflection usually occurs best when the sample has a rough surface.

In the case of a skin tissue, when a collimated light source impinges on the skin, the light is scattered within the skin structures in a way that obeys the Mie scattering [17], [45]. The light will be absorbed by primarily blood, melanin and water in skin. Therefore, as it is diffusely reflected out of the media and captured by a detector, such as a camera, the absorption and scattering parameters is encoded within the image. The parameters can then be extracted when it is fitted to a model [36], [47].

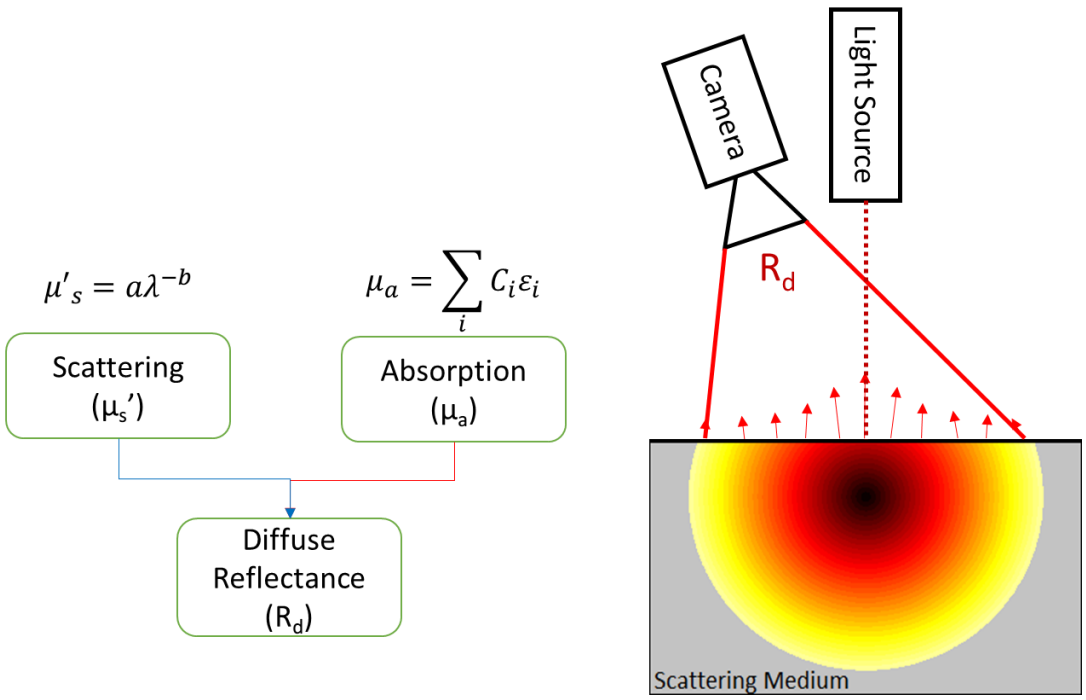


Figure 2.17. The diffuse reflectance is collected with a camera. It is a function of the scattering and absorption parameters.

# CHAPTER 3: SPATIAL FREQUENCY DOMAIN IMAGING

## 3.1 Introduction

Accurate separation and quantification of absorption and scattering parameters remains a challenge in optical imaging. This is due to the complex interactions between light and the medium of interest, where absorption and scattering often happen simultaneously [10], [36], [53]. To do this, there are generally two approaches. The first approach is using time resolved measurements [55]–[58]. Light transport can be approximated by a point spread function in the real domain with a collimated light source. When the incident temporal point spread function (t-PSF) is plotted as a function of time – typically in the range of a few nanoseconds – a gap is seen before a sudden peak of photons arriving, followed by an exponential decay (Figure 3.1). Within time resolved measurements, another approach is to look at the frequency domain [59]–[61]. In the frequency domain, the experimental variable is the temporal modulation transfer function (t-MTF), which is a function of frequency – typically in gigahertz. In this domain, the attenuation and the phase delay of a periodically varying photon density wave is measured, which resembles an inverse exponential curve. This is expected, as the t-PSF is also the Fourier transform equivalent of the t-MTF.

The second approach to extract the absorption and scattering coefficients is through spatially resolved measurements, which often necessitates the measurement of intensity at different separation distance [10], [18], [19], [45]. This approach is similar to the time resolved measurements except that the point spread function is measured

spatially instead of temporally, and hence the spatial point spread function (s-PSF) is a function of the distance away from the incident source – typically in mm to a few cm. The curve also follows an exponentially decaying response **(**Figure 3.1**).** Similarly, the Fourier transform of the s-PSF is equivalent to the spatial modulation transfer function (s-MTF) in the spatial frequency domain (SFD) which produces a sigmoidal liked curve. Measurements in the SFD have advantages, especially in the clinical environment due to the cost of the physical hardware, ability to generate wide field optical maps of absorption and scattering and the minimal use of moving parts.

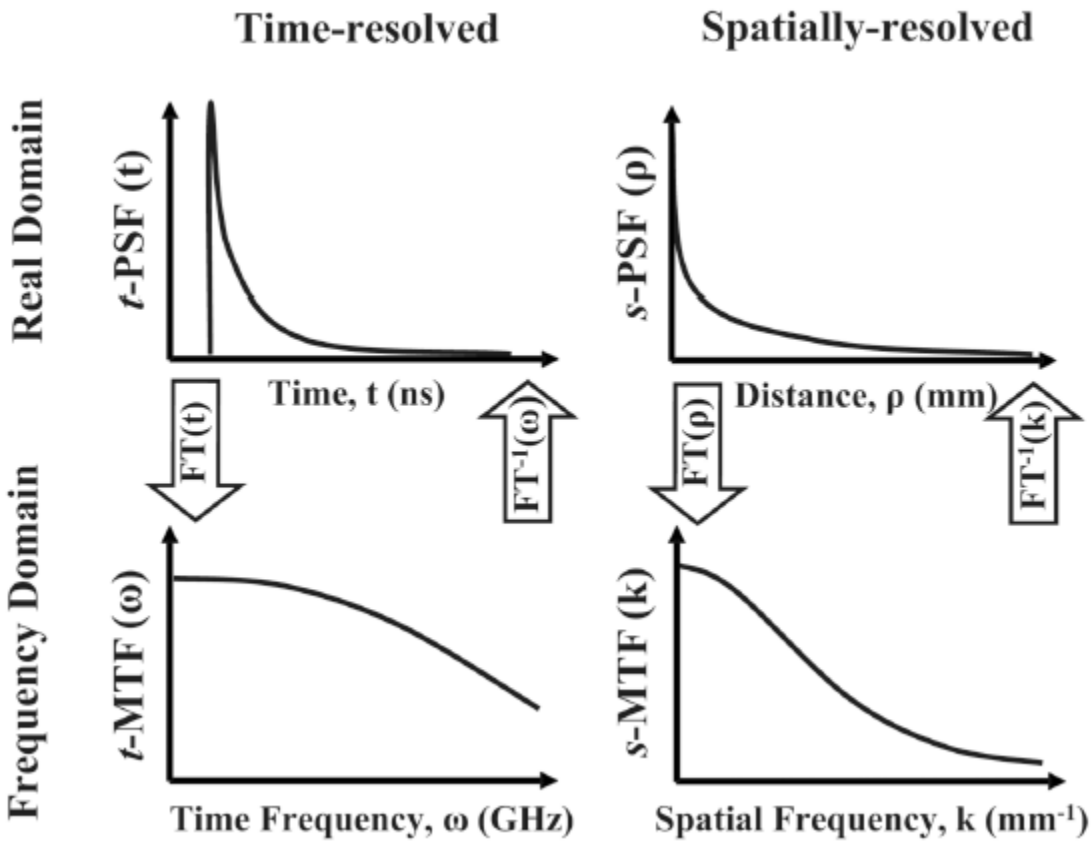


Figure 3.1. Light transport in different measurement domains when it is in a turbid media. Light transport can be measured temporally or spatially, in the real domain or the frequency domain. The real domain and frequency domain is Fourier Transform equivalent of each other. Retrieved from [10]

Spatial frequency domain imaging (SFDI) is a novel wide field, non-contact and non-ionizing imaging modality [10]–[16], [20], [62]–[66]. When SFDI is performed with multiple wavelengths, it is possible to decompose the absorption parameter into its respective components (oxy-hemoglobin, deoxy-hemoglobin, melanin, water), and therefore approximate the vascular contrast (tissue oxygenation saturation and blood volume) [12]–[16], [62], [63], [66]. In addition, the scattering parameter can be decomposed into properties such as "scatterer" size and density (Figure 2.11), which provides structural information about the tissue.

## 3.2 Diffusion Equation Approximation in the Spatial Domain

An analytical model based on the diffusion equation in a turbid media for SFDI as derived by Cuccia et al is frequently used to quantify the optical properties of a sample [10], [67]–[69]. This phenomenon is well established and has been widely used in the field of biomedical optics, although it is developed more specifically for the case of s-PSF as a function of spatial distance. Theoretically, it has been long understood that the Fourier transform of the s-PSF is equivalent to the s-MTF, however, practically this approach of spatially modulating the source has not been studied until recent years [10].

To start, the well-established diffusion equation (2.1) in an infinite homogenous medium can be re-written in a time independent form to give:

$$\nabla^2\varphi - \mu_{eff}^2\varphi = -3\mu_{tr}q \tag{3.1}$$

where φ is the fluence rate, q is the source, $\mu_{tr}$ is the transport coefficient and $\mu_{eff}$ is the attenuation coefficient. A normally incident, periodic plane wave source in a semi-infinite geometry can be represented by:

$$q = q_0(z)\cos(k_x x + \alpha) \tag{3.2}$$

where α are the spatial phase shifts in the respective directions and spatial frequencies are $k_x = 2\pi f_x$. When the response of the medium is proportionate to the input intensity this equation will yield:

$$\varphi = \varphi_0(z)\cos(k_x x + \alpha) \tag{3.3}$$

Combining the diffusion equation (Eqn (3.1)) and the modulated light source (Eqn (3.3)) creates a partial differential equation with the fluence rate as a function of depth, z:

$$\frac{d^2\varphi_0(z)}{dz^2} - \mu_{eff}'^2\varphi_0(z) = -3\mu_{tr}q_0(z) \tag{3.4}$$

where

$$\mu_{eff}' = \sqrt{\mu_{eff}^2 + k_x^2} \equiv \frac{1}{\delta_{eff}'} \tag{3.5}$$

Here, $\delta'_{eff}$ is the effective penetration depth where it is equivalent to the illumination source when spatial frequency, $k = 0$ (DC). Since Eqn (3.4) is a function of only depth and not in the x direction, $\mu_{eff}$ is substituted with $\mu'_{eff}$ (Eqn (3.5)) to account for the modulated scalar attenuation in the x direction.

Following the derivation of Cuccia et al. the diffuse reflectance, $R_d(k)$ can be obtained from the following equation:

$$R_d(k) = \frac{3Aa'}{(\mu'_{eff}/\mu_{tr} + 1)(\mu'_{eff}/\mu_{tr} + 3A)} \tag{3.6}$$

where *a'* is the reduced albedo, *A* is the proportionality constant.

$$a' = \mu'_s/\mu_{tr} \tag{3.7}$$

$$A = \frac{1 - R_{eff}}{2(1 + R_{eff})} \tag{3.8}$$

$$R_{eff} \approx 0.0636n + 0.668 + \frac{0.710}{n} - \frac{1.440}{n^2} \tag{3.9}$$

Here, $R_{eff}$ is the effective reflection coefficient, n is the refractive index of tissue.

Using Eqn (3.6), the diffuse reflectance of the reference can be modeled and fitted to quantify the diffuse reflectance of the sample. However, it is also important to take note that the diffusion approximation to the radiative transport equation is valid when:

$$\mu'_s \gg \mu_a \tag{3.10}$$

## 3.3 Spatial Frequency Projection and Demodulation

By separating the DC and AC components of spatially modulated light, the s-MTF of the system can be obtained when it is plotted as a function of the spatial frequency (Figure 3.2).

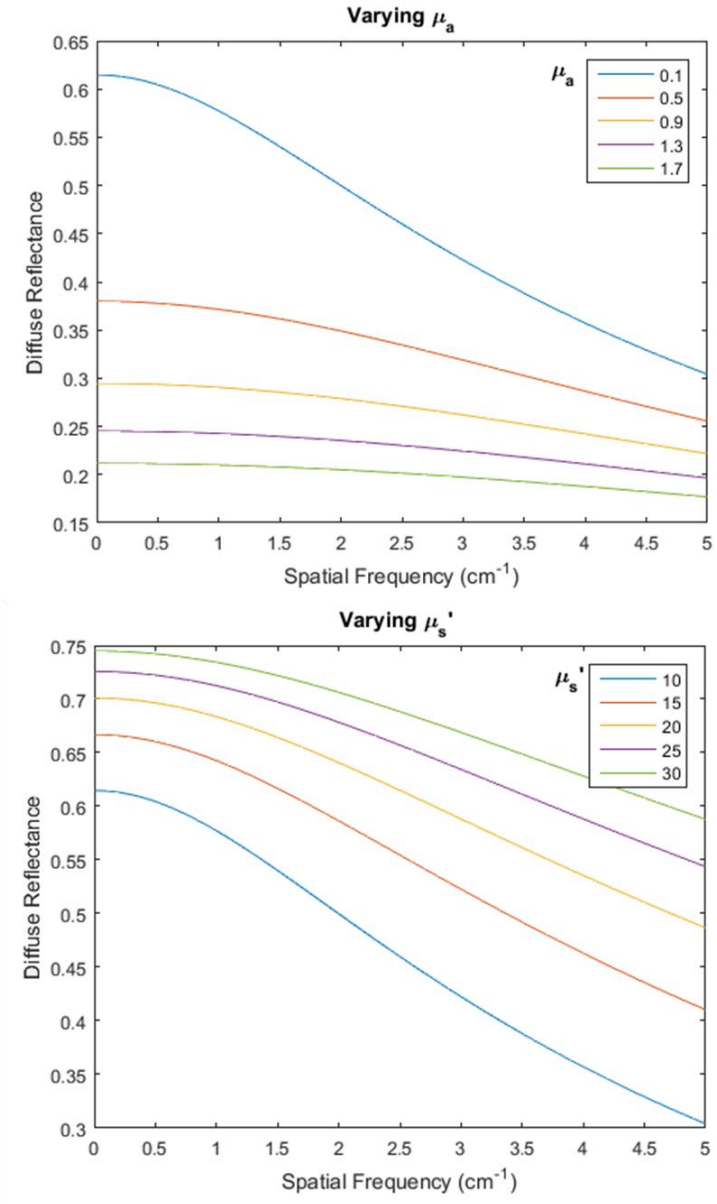


Figure 3.2. Changes in the s-MTF when absorption and scattering is increased. Values are all in cm$^{-1}$. In both cases, the initial values of absorption and scattering (blue line) was fixed at (0.1cm$^{-1}$, 10cm$^{-1}$) respectively.

In the case of a simple sine wave modulation in the x-axis, the modulation waveform, *m(x)*, of spatial frequency, $f_x$ is given by:

$$m(x) = M_0 \cdot cos(2\pi f_x x + \alpha) \tag{3.11}$$

where $M_0$ and $\alpha$ are the modulation depth and the spatial phase respectively. However, in practice it is impossible to modulate the AC component with a negative scalar intensity, so the AC component has to be super positioned at the DC component [10]. This modifies the equation to be as follows:

$$S(x) = \frac{S_0}{2}[1 + M_0 \cdot \cos(2\pi f_x x + \alpha)] \tag{3.12}$$

where $S_0$ is the source intensity. Therefore the components of reflected intensity, *I*, are:

$$I = I_{AC} + I_{DC} \tag{3.13}$$

Since only the AC component is modulated

$$I_{AC} = M_{AC}(x, f_x) \cdot \cos(2\pi f_x x + \alpha) \tag{3.14}$$

where $M_{AC}$ is the amplitude of the reflected modulated intensity at frequency $f_x$.

To reverse the amplitude modulation, a simple approach is by illuminating the sinusoidal pattern at three different phase offsets (0, 2π/3, 4π/3) at the same spatial frequency (Figure 3.3) [10], [62], which then $M_{AC}$ can be recovered by:

$$M_{AC}(x_i, f_x) = \frac{\sqrt{2}}{3}\sqrt{[I_1(x_i) - I_2(x_i)]^2 + [I_2(x_i) - I_3(x_i)]^2 + [I_3(x_i) - I_1(x_i)]^2} \quad (3.15)$$

where $I_1$, $I_2$, $I_3$ represents the reflected intensity image at different phase offsets respectively.

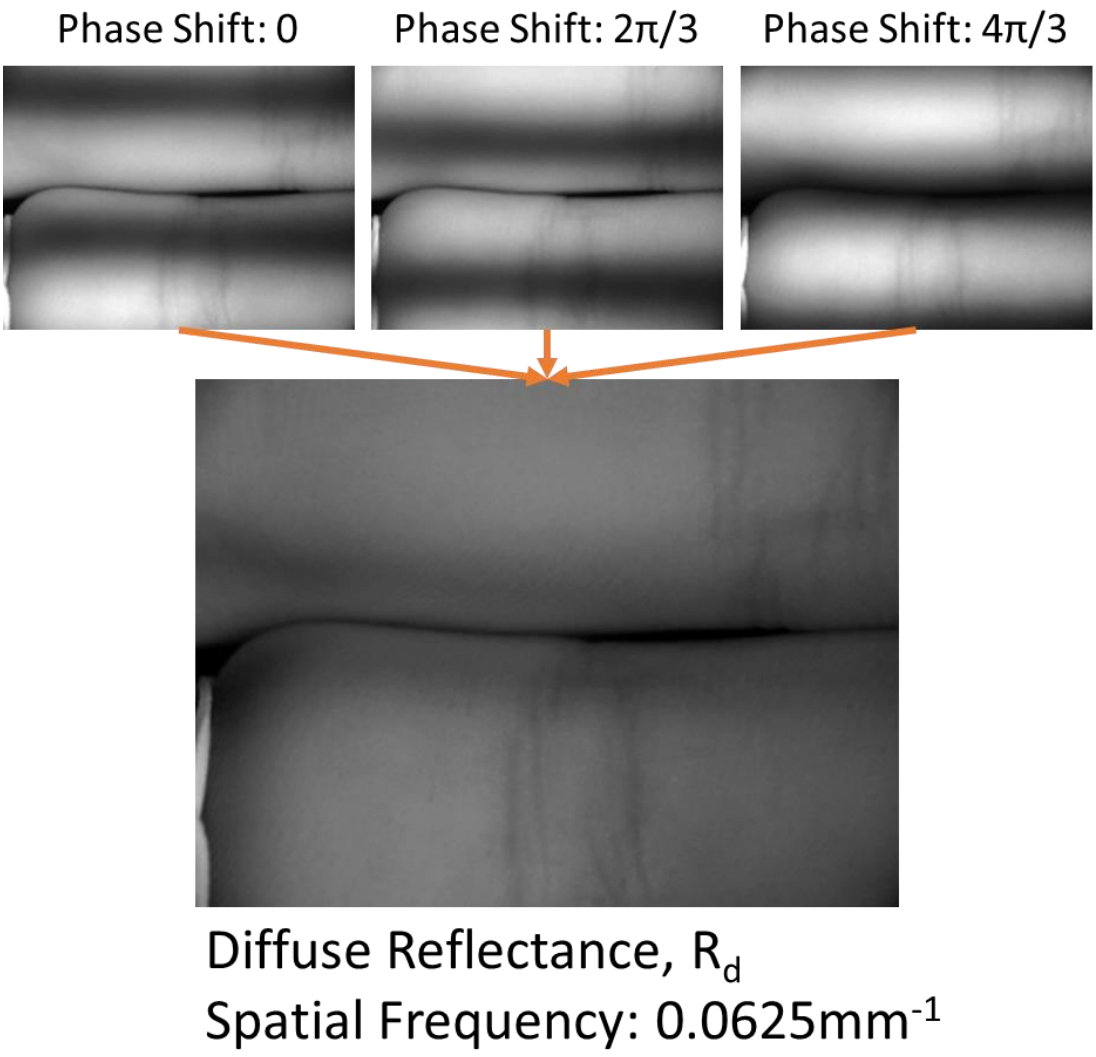


Figure 3.3. Amplitude modulation and demodulation of an image of two fingers. The light captured with a camera that is modulated with three phases (0, 2π/3, 4π/3) can be recovered by combining the DC and AC components.

The $M_{DC}$ can also be obtain with the following equation:

$$M_{DC}(x_i) = \frac{1}{3} \cdot [I_1(x_i) + I_2(x_i) + I_3(x_i)] \tag{3.16}$$

$M_{AC}$ is also composed of the product of three components. They are the source intensity, MTF of the system and the diffuse reflectance, $R_d$, which is the MTF of the sample. In the case of a turbid media, such as the human skin, we expect it to look like an inverse sigmoidal curve (Figure 3.4), as seen in (Figure 3.1).

$$M_{AC}(x_i, f_x) = I_0 \cdot MTF(x_i, f_x) \cdot R_d(x_i, f_x) \tag{3.17}$$

The equation can be further simplified with the use of a reference phantom with known optical properties, since the source intensity, $I_0$, and the amplitude of the reflected modulated intensity, $M_{AC}$, are similar in both cases.

$$R_d(x_i, f_x) = \frac{M_{AC}(x_i, f_x)}{M_{AC,ref}\,(x_i, f_x)} \cdot R_{d,ref}\,(f_x) \tag{3.18}$$

Where $M_{AC,ref}$ is the amplitude of the reflected modulated intensity of the reference and the $R_{d,ref}$ is the diffuse reflectance of the reference that can be predicted when fitted to a model.

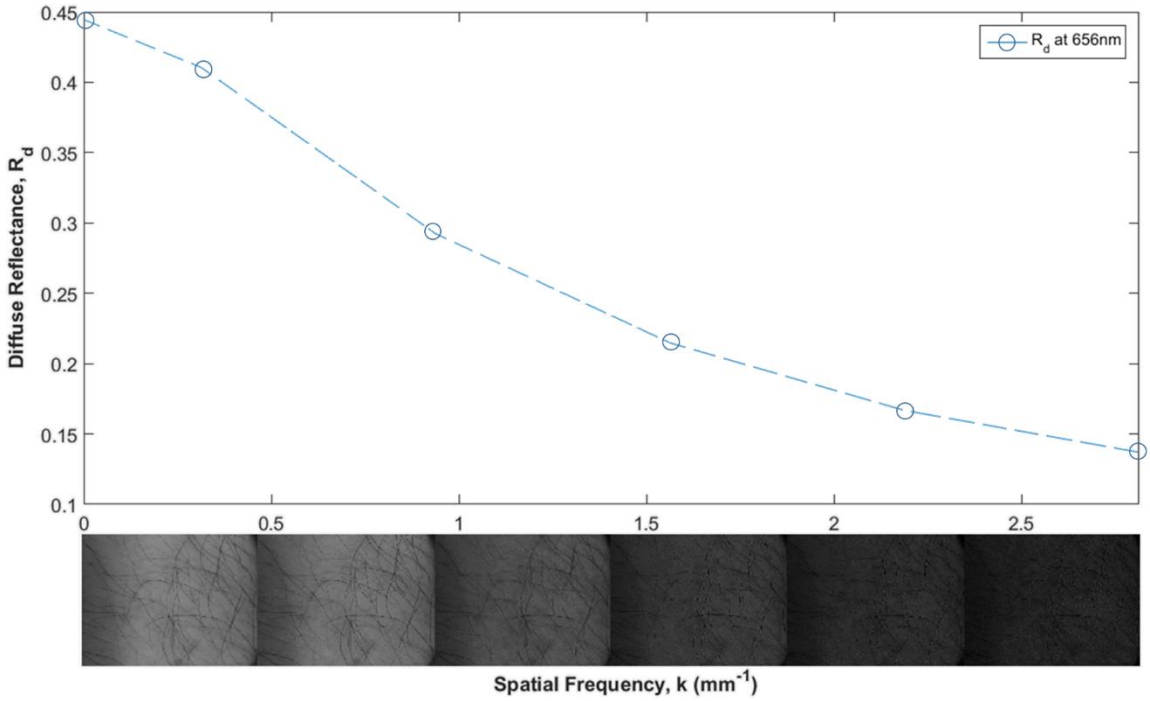


Figure 3.4. *In vivo* diffuse reflectance curve of a human skin. The characteristic exponential decay curve as a function of spatial frequency is seen here. The optical properties are approximated by calibrating against and fitting the diffuse reflectance of a known reference.

## 3.4 Optical Properties Quantification

The optical properties of the sample can be quantified from the diffuse reflectance, $R_d$, with the use of a known reference as seen in Eqn (3.18). Since both $M_{AC}$ and $M_{AC,ref}$ can be obtained experimentally, the remaining unknown parameter in the equation is the diffuse reflectance of the reference, $R_{d,ref}$. There are generally two approaches to obtain $R_{d,ref}$, the first being the Monte Carlo approximation and the second being the diffusion equation approximation [36], [47]. Both methods generate the $R_{d,ref}$ at

each spatial frequency, to which the diffuse reflectance of the sample can be quantified relative to the input reference optical properties.

Typically, Monte Carlo simulations are computationally intensive. To reduce the computation time, the simulations are performed well in advance of measurements and stored into a lookup table, where $R_{d,ref}$ can be retrieved to fit for the $R_d$ of the unknown sample [10], [65]. To reduce the computation time further, a faster approach based on this method, is described by Cuccia et al. to fit for a single, however, these approaches would not be discussed in detail [10], [70], [71].

## 3.5 SFDI Instrumentation

We have built an SFDI system that utilizes multiple interchangeable collimated light emitting diodes (LED) with a center wavelengths of 490nm, 590nm, 660nm and 780nm (LCS series, Mightex, Toronto, Ontario, Canada) that are sequentially selected with a four channel LED controller (SLC-SA04-US, Mightex, Toronto, Ontario, Canada). Depending on the application, the LEDs can be switched out accordingly, and can be expanded to more than four wavelengths if necessary. The LED light is focused into a liquid light guide and expanded onto a digital micro-mirror device (DMD) (DLP LightCrafter 4500, Texas Instruments, Dallas, TX) that has 912x1140 pixel resolution. It modulates the amplitude of the incoming light with a sine wave at the specified spatial frequency depending on the application. Each frequency is projected at three phases (0, $2\pi/3$, $4\pi/3$) onto the target. A scientific camera (Zyla, Andor Technology, Belfast, United Kingdom) is then used to capture the resulting image with a 4cm x 3cm field of view.

The projected light and the incoming light are cross-polarized to reduce specular reflections. A light shield with a window for imaging was also 3D printed to reduce external stray lights and maintain the same focal plane in subsequent measurements (Figure 3.5).

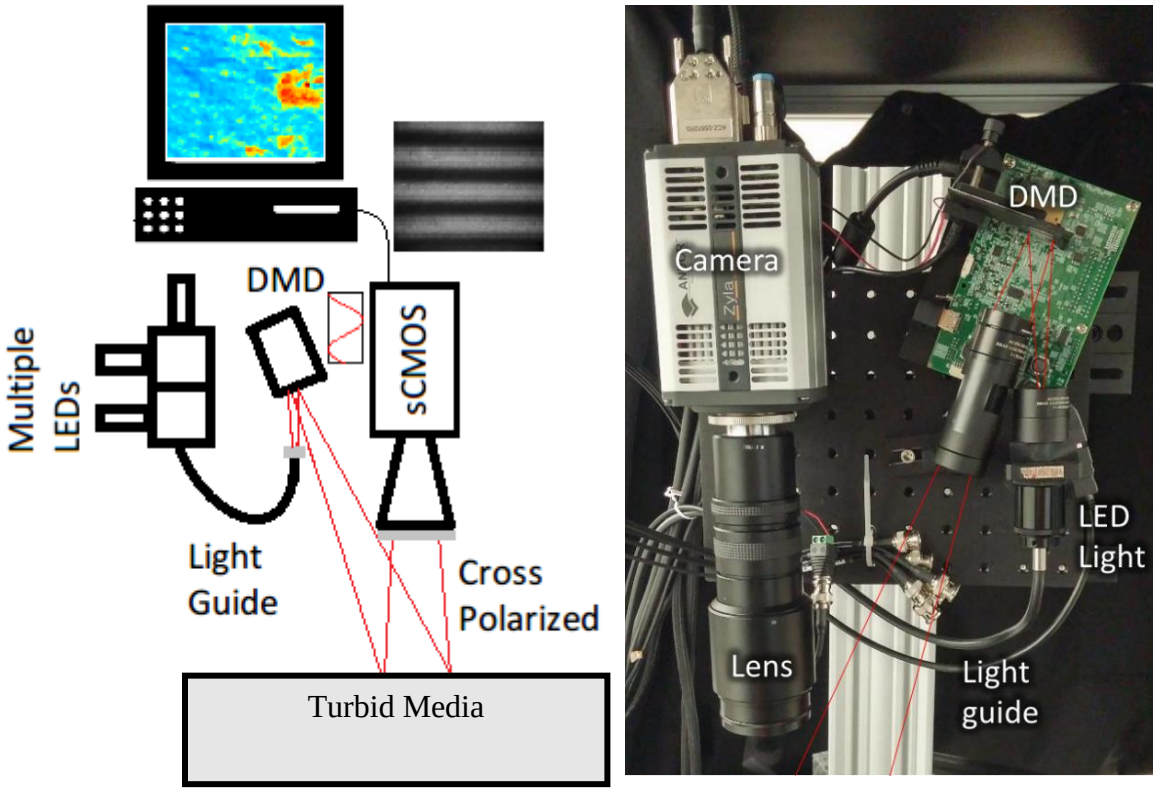


Figure 3.5. Instrumentation of our SFDI setup. The sample is projected with a LED at a specified center wavelength that is modulated with a DMD at different spatial frequencies. The image is the cross-polarized to eliminate specular reflection and collected with a sCMOS camera. The data is then demodulated and processed with a computer

The data were analyzed with a custom program using MATLAB. The images were demodulated and calibrated against the reference to obtain the diffuse reflectance image at each spatial frequency. A pixel-by-pixel fitting with the diffusion equation approximation (Section 3.2) is used with the spatial modulation transfer function to extract the optical properties of the sample (Figure 3.6). To obtain the hemoglobin parameters, absorption was decomposed into four components (Figure 2.13). It was fitted using the analytical diffusion equation with the spatial modulation transfer function and scattering property as an input. The total hemoglobin concentration and the blood-oxygenation saturation maps can then be calculated. To obtain the scattering parameter, a, and, b, scattering is modeled and fitted according to Mie scattering ($\mu_s' = a\lambda^{-b}$), which produces a "scatterer density" map and a "scatterer size" map (Figure 2.11).

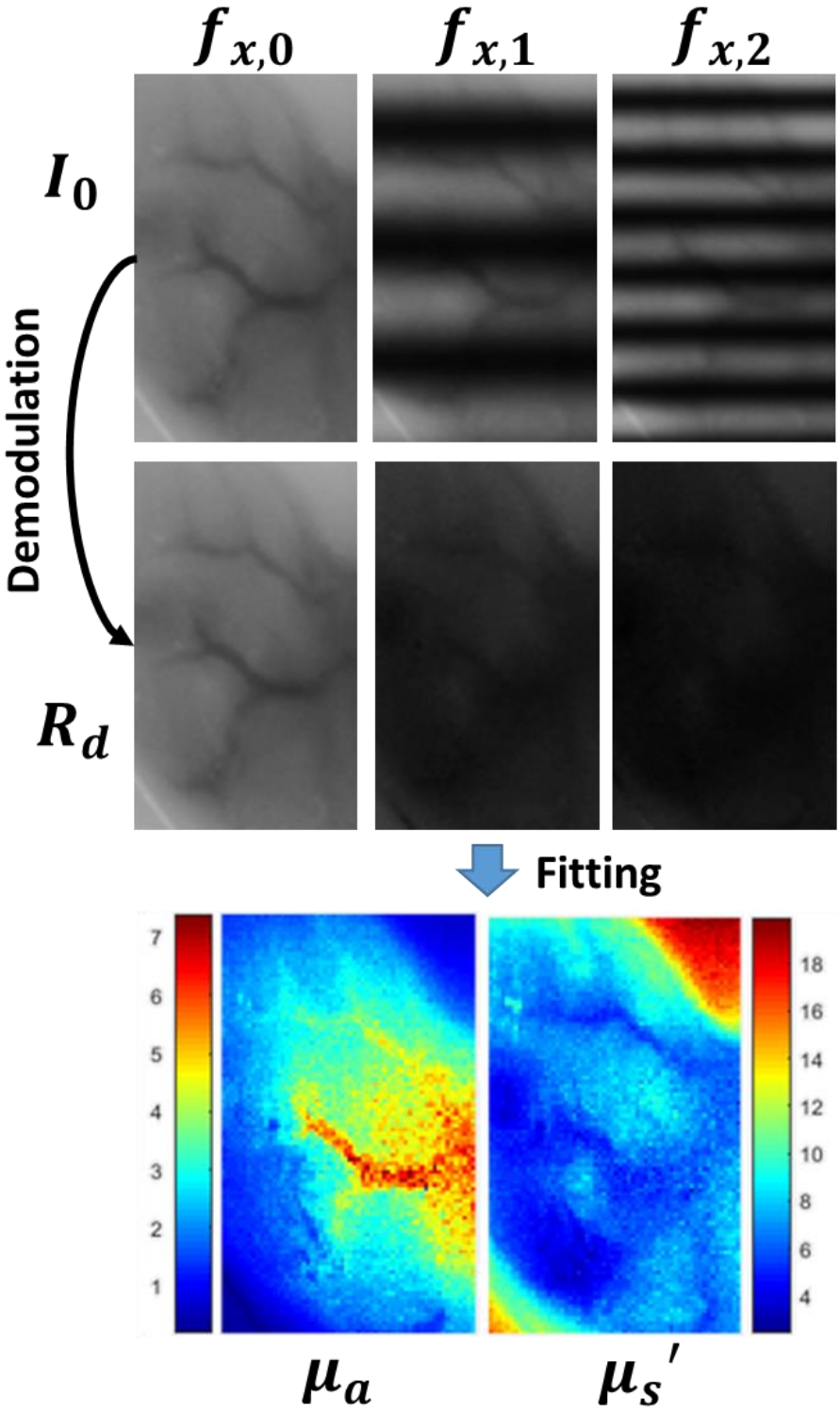


Figure 3.6. The images are demodulated to obtain the diffuse reflectance image at each spatial frequency. They are then fitted with the diffusion model to obtain a map of the optical parameters.

## 3.6 SFDI Calibration

Theoretically, SFDI is able to quantify the optical properties of an unknown media based on a known reference point [10]. However, experimentally, there are still errors with the quantification that can arise due to experimental inconsistencies [68]. One of the major experimental inconsistencies is the height variation. To overcome this problem, a light shield with an imaging window is implemented to fix the height, so that the sample will always be in focus when it is in contact with the imaging window. To make sure that the system can correctly quantify the optical properties, two phantoms with known properties were measured relative to each other.

### 3.6.1 Phantom Preparation

To validate and calibrate the system, we used two solid phantoms made with Polydimethylsiloxane (PDMS) [27], which is a rubber-liked solid phantom with a physical dimension of 10 x 10 x 3cm to stimulate human skin. This solid phantom was made with titanium dioxide ($TiO_2$) as the scattering agent. $TiO_2$ was used as it has a negligible absorption coefficient and has a particle size (~100nm) within the visible wavelength of light for modeling Mie scattering (Figure 2.15) [27], [72]–[74]. India ink was used as the primary absorbing agent as it has negligible scattering coefficients due to small particle size and high absorption [27], [73], [75]. The phantoms were made to have an optical property close to human skin with two different absorption values to stimulate normal and burned skin (Table 3.1) [12], [13], [27].

Alternatively, a liquid phantom can be made with Intralipid – a widely used intravenous lipid supplement – as the scattering agent and India ink as the absorption agent [75]–[77]. Liquid phantom can be prepared easily; however, they have a limited shelf life [27]. The PDMS phantoms are quantified with a commercial system (Integrating Sphere System) to obtained mean absorption and scattering over a spectral range of 400-1100nm at ~2nm spectral resolution (Figure 3.7). The surface was also sanded to reduce specular reflection. The final optical properties of the phantoms are close to the expected value with an error of less than 5% (Table 3.1).

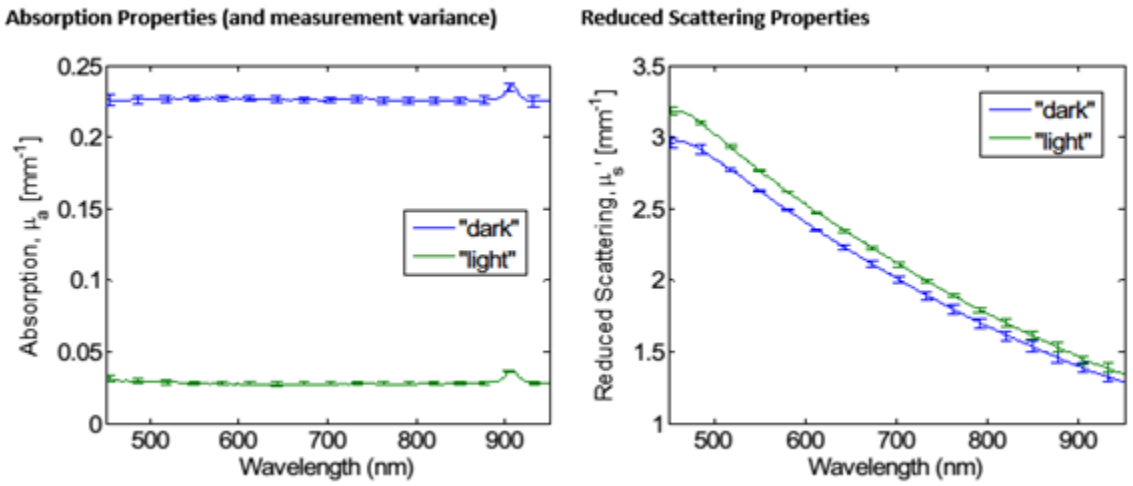


Figure 3.7. Optical properties spectra of two separate PDMS phantoms used to stimulate normal and burned skin.

Table 3.1. Actual and estimated optical properties of the two PDMS phantoms

| | $\mu_{s',\ Light}$ | $\mu_{a,\ Light}$ | $\mu_{s',\ Dark}$ | $\mu_{a,\ Dark}$ |
|---|---|---|---|---|
| **Actual (700nm)** | $20cm^{-1}$ | $0.3cm^{-1}$ | $20cm^{-1}$ | $2cm^{-1}$ |
| **Estimated (700nm)** | $21.27cm^{-1}$ | $0.2746cm^{-1}$ | $20.14cm^{-1}$ | $2.263cm^{-1}$ |
| **Total Error (%)** | 0.89% | 2.1% | 1.2% | 0.91% |

## 3.6.2 SFDI Phantom Testing

Both phantoms were imaged with three wavelengths, six spatial frequencies (0 – $0.28mm^{-1}$), three phases and three dark counts, resulting in 57 images. The dark counts were subtracted with all the images within the same wavelength. The three phases were then demodulated to obtain a diffuse reflectance image at each spatial frequency. The images were stacked in the third dimension, where each pixel is extracted as a function of spatial frequency and fitted with the diffusion equation, using the non-linear least squares fitting routine in Matlab. The dark phantom was used as a reference to the "unknown" light phantom. Since the phantoms were homogenous, it is binned to 25 x 25 pixels for faster processing.

The initial results obtained from the system were found to be off by a constant factor of 0.74 for $\mu_s$', while $\mu_a$ was found to be within the expected range. This factor was used to calibrate the system so that the final value was close to what was expected. In the

final set of results, all results are within the range of the expected result with an error of less than ~5% away from the expected mean (Table 3.2).

Table 3.2. Results obtained from imaging the light phantom with SFDI after calibration.

| | $\mu_{s'}$, Expected | $\mu_{s'}$, Result | $\mu_a$, Expected | $\mu_a$, Result |
|---|---|---|---|---|
| **490nm** | 30.72cm$^{-1}$ | 30.26 ± 2.30cm$^{-1}$ | 0.2986cm$^{-1}$ | 0.2987 ± 0.0469cm$^{-1}$ |
| **590nm** | 25.70cm$^{-1}$ | 25.86 ± 1.67cm$^{-1}$ | 0.2772cm$^{-1}$ | 0.2709 ± 0.0367cm$^{-1}$ |
| **656nm** | 22.92cm$^{-1}$ | 24.11 ± 1.16cm$^{-1}$ | 0.2730cm$^{-1}$ | 0.2613 ± 0.0311cm$^{-1}$ |

# CHAPTER 4: NON-CONTACT QUANTIFICATION OF BURN SEVERITY IN EXCISED HUMAN TISSUE

## 4.1 Introduction

Application of SFDI to different animal models (porcine and rat) has already been performed by several groups [12], [13], [78]. Live models simulates the internal environment of a burn wound more accurately, but it also introduces different variables such as blood flow, inflammation and wound healing that may vary across different species. Here, we are primarily interested in optical properties changes due to cellular and structural transformation caused by burn damage. To our knowledge, this is the first application of SFDI to burn severity resolution in *ex vivo* human skin. To test our hypothesis, we obtained de-identified skin samples from patients that had just undergone abdominoplasty and burned them with a heated metal block to induce various grades of burn. The samples were imaged with SFDI to quantify the optical properties, and were immediately biopsied after the optical measurements. This was done so that the histological analysis of the biopsy would quantify the burn depth, which could then be compared to the optical measurements (Figure 4.1), more specifically, the scattering parameter, b. With this in mind, we hope to create a simple model where SFDI is able to characterize thermal burn injuries, and adapt it for use in other environmental injuries to include caustic agents and vesicants.

## 4.2 Methods

To perform this experiment, a skin sample was obtained and burned with a metal block for various lengths of time to simulate different grades of burn. Next, SFDI was used to image the samples with a field of view of ~4cm x 3cm. Immediately after imaging, a biopsy was taken from the sample, which was sent to a dermatopathologist to perform histological analysis. The SFDI images were analyzed to obtain the optical properties. Results from SFDI were compared to burn depth as measured with histology to obtain a simple model for characterizing burn severity (Figure 4.1). These will be discussed in details in the following sections.

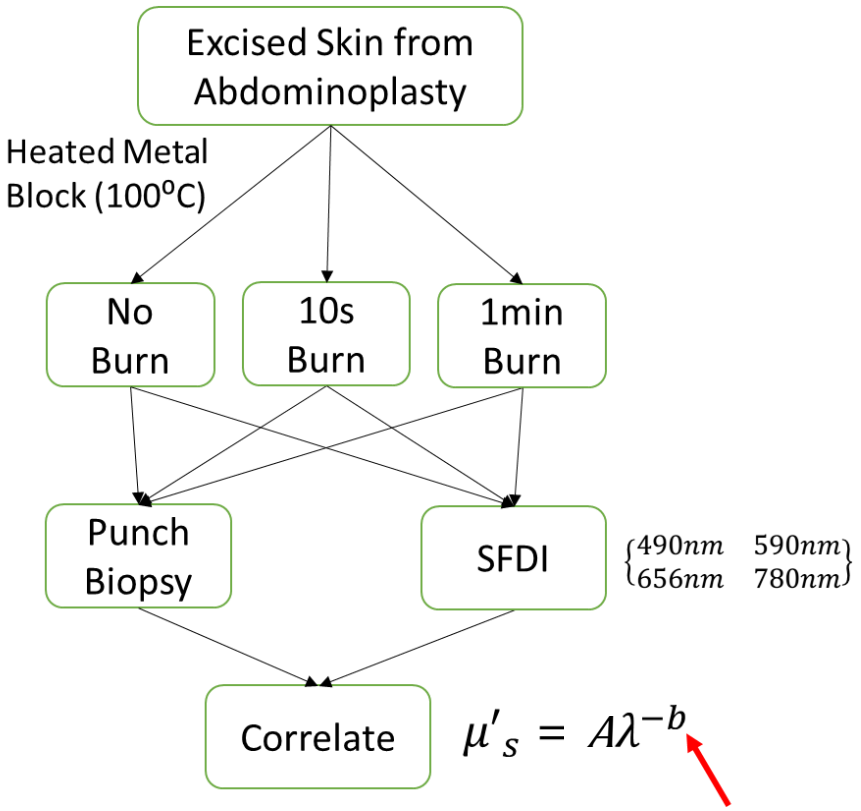


Figure 4.1. The skin is treated with different duration of burn to simulate different grades of burn. The results from histological analysis that is obtained with punch biopsy, is correlated with the changes in optical properties obtained with SFDI, specifically, the scattering parameter b.

### 4.2.1 Skin Preparation and Burn Model

*Ex vivo* de-identified skin was obtained from patients that had just undergone abdominoplasty. The skin was separated into three equal pieces of ~10 x 10cm squares. Burn was induced on the skin by placing metal blocks that were heated to 100°C with boiling water. The heated metal block was placed on the first sample for 10 seconds to induce a grade II burn (Figure 4.2a). For the second sample, two metal blocks were heated. The first block was placed on the skin surface for 30 seconds and immediately switched out with the second block for another 30 seconds to apply constant heat to induce a grade III burn. The last sample was used as a control, so it was left unburned. The skin samples were all imaged within the first hour post burn.

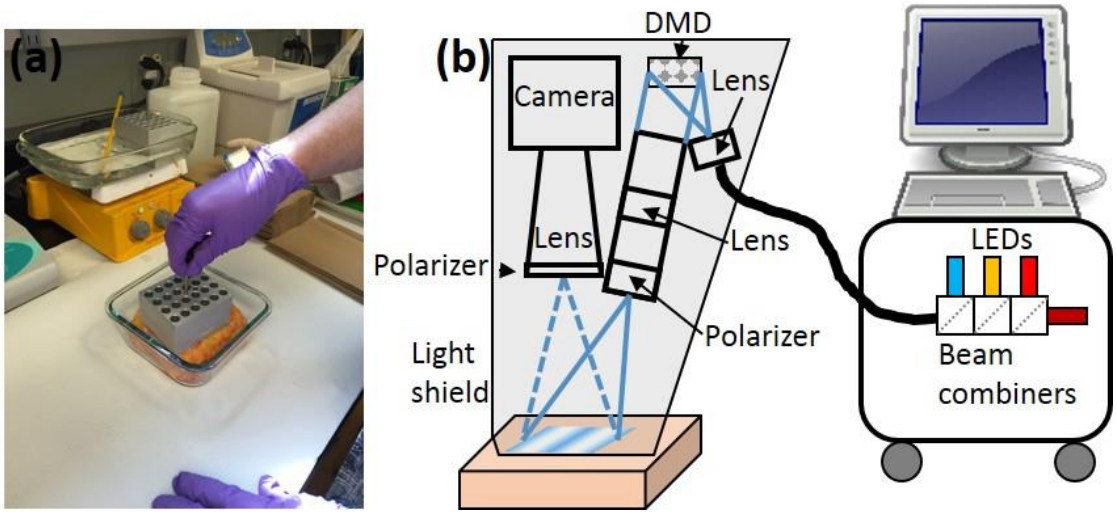


Figure 4.2. (a) Picture of skin being burned. (b) Schematic of setup

### 4.2.2 SFDI Instrumentation

The samples were placed on a tray and raised with a positioner so that it would come in contact with the imaging window on the light shield. A visually smooth area, free of cellulite, was marked with a pen and oriented so that it would be centered on the bottom of the image. The LEDs, DMD and camera were all controlled by a custom written LabVIEW software, to acquire the whole set of 136 images (four wavelengths ( Figure 4.1), 11 spatial frequencies (0 – 0.44mm$^{-1}$), three phases, four dark counts) in under 2.5 minutes. The image was also taken in a dark enclosed area to reduce stray light. Immediately after imaging, a punch biopsy was taken. This process was repeated for all three samples. After the samples were imaged, a liquid phantom (Section 3.6.1) with known optical properties was made with intralipid as the scattering agent and India ink as the absorption agent. These phantom images serve as a reference for the samples as described in (Section 3.2).

### 4.2.3 Image Analysis

A custom routine was written in Matlab to analyze the images obtain from SFDI. The first six spatial frequencies (0 to 0.22 mm$^{-1}$) were used, where the three phases of each spatial frequencies were demodulated to obtain six two-dimensional diffuse reflectance image [10]. The six images were stacked together on the third dimension, which allows an s-MTF to be generated for each pixel as a function of spatial frequency (Figure 4.3).

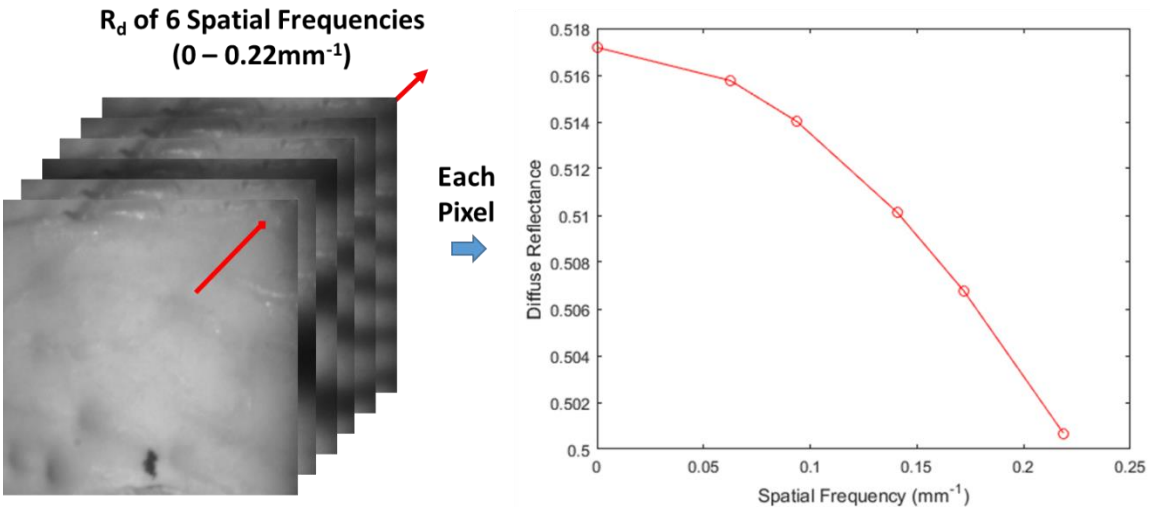


Figure 4.3. The diffuse reflectance images were stacked in 3D as a function of spatial frequencies. Each pixel produced an s-MTF to fit the model so that the optical properties map can be obtained.

A model was used to fit against the s-MTF so that the optical properties can be quantified at the pixel level. This process was repeated for all four wavelengths and for each of the three samples. Since we were interested in the structural changes caused by burn, the scattering parameter, b, which is related to the "scatterer" size, was our quantity of interest. We used the Mie scattering behavior (Figure 2.14), where $\mu_s' = A(\lambda/\lambda_0)^{-b}$ and λ0 is the normalization wavelength (700 nm) to model the $\mu_s$' at each pixel to obtain a map of the scattering parameters A and b.

### 4.2.4 Histopathology

After optical measurements, 6 mm punch biopsies were taken from the area that coincides with the center of the imaging area, which is approximately 1.5cm above the mark. The tissue sample was fixed with formalin for one hour, and stored in 70% ethanol. The tissue was embedded in paraffin, cut into 5-micron thick sections, and stained with hematoxylin and eosin. The biopsies were imaged with light microscopy to assess for thermal injury and read independently by two dermatopathologists in a blinded fashion. The depth of injury was measured in millimeters from the basement membrane to the deepest extent of the dermal connective tissue alteration using an ocular micrometer. Values are reported as the mean and standard deviation.

## 4.3 Results

Four human skin samples were burned *ex vivo* with either a 10-second or a 60-second thermal injury (Fig 1a). As shown in (Figure 4.4), the thermal injury resulted in distinct histologic changes including epidermal blistering and swelling/degradation of dermal collagen. The depth of dermal damage was easily visualized using hematoxylin and eosin staining. The control sample (Figure 4.4a) showed no damage while the 10 and 60 second burn samples (Figure 4.4b-d) showed noticeable damage. As noted in (Figure 4.4d), the 60-second injury resulted in full dermal damage. Measuring the distance from the basement membrane to the extent of the damage resulted in values of 1.15 +/- 0.07 mm for the 10 second injury and 4.1 +/- 0.5 mm for the 60 second injury (mean +/- SD; N = 4). These findings indicate that our injury model results in a reliable damage

response.

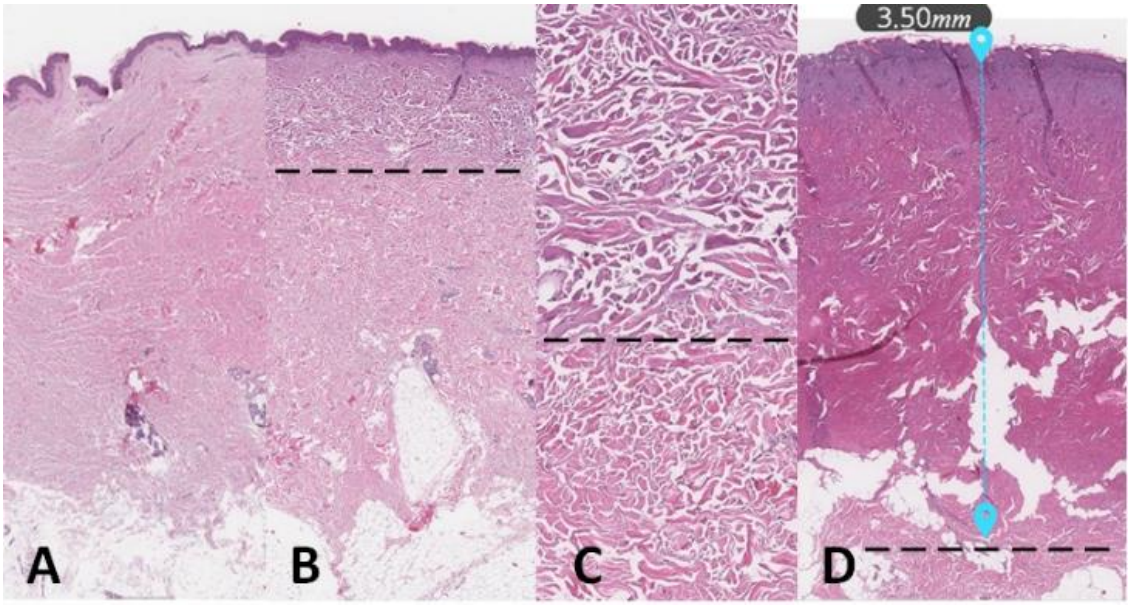


Figure 4.4. Burn depth assessed with histology. (a) Control; (b) 10 second burn; (c) high-power view of dermis in the 10 second burn; (d) 60 second burn. Dotted lines denote changes in collagen indicating burn depth.

Representative optical property maps from one sample are shown in (Figure 4.5a) and (Figure 4.5b). Both the short and long duration burns showed changes in absorption and scattering parameters compared to control. At all four wavelengths, the absorption increased with burn duration, while scattering increased for 490nm and decreased at the other wavelengths. (Figure 4.6a) and (Figure 4.6b) summarize the wavelength dependency of the absorption and scattering parameters respectively. The plots show the mean and standard deviation of all samples.

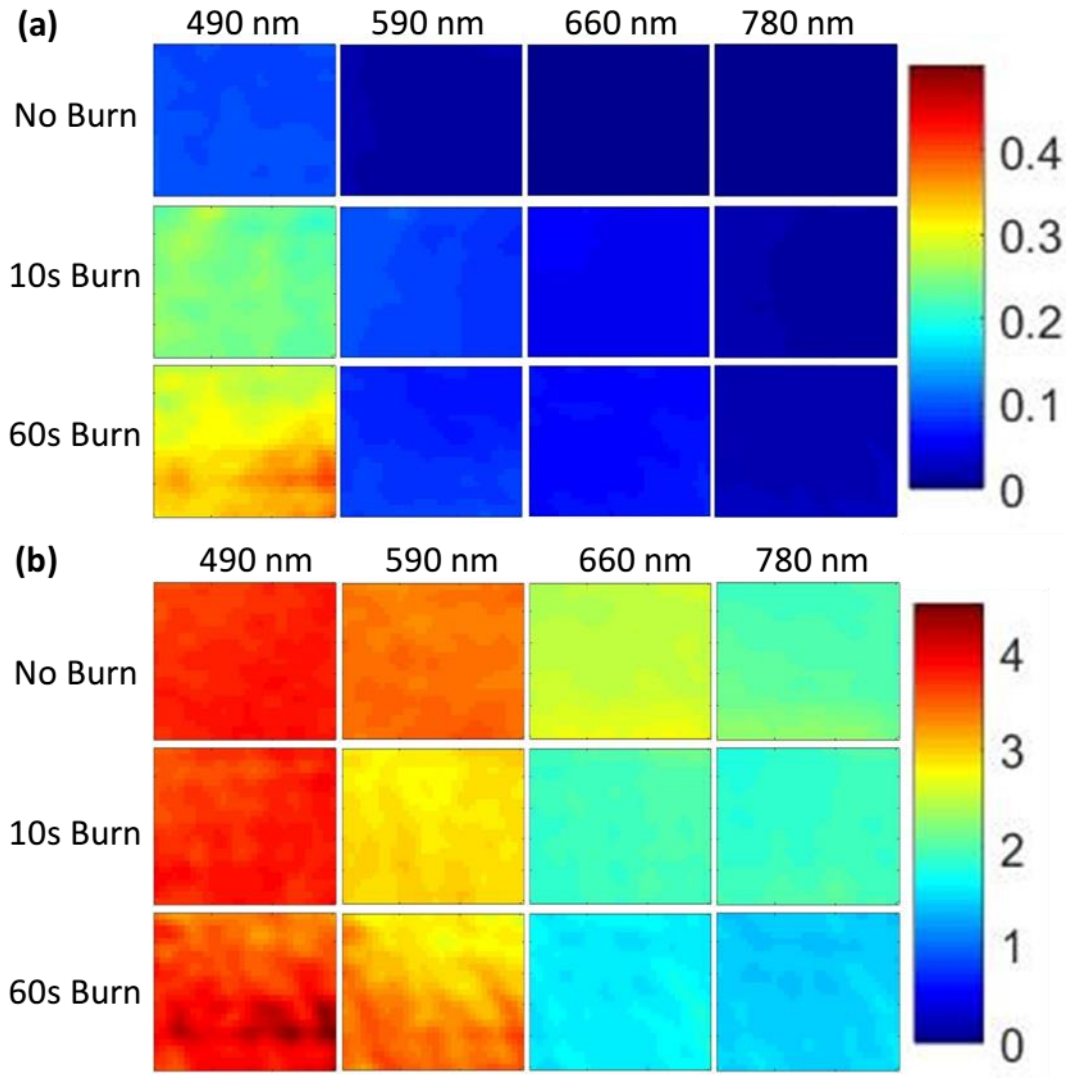


Figure 4.5. Optical property maps for one sample. (a) absorption, $\mu_a$, and (b) scattering, $\mu_s'$.

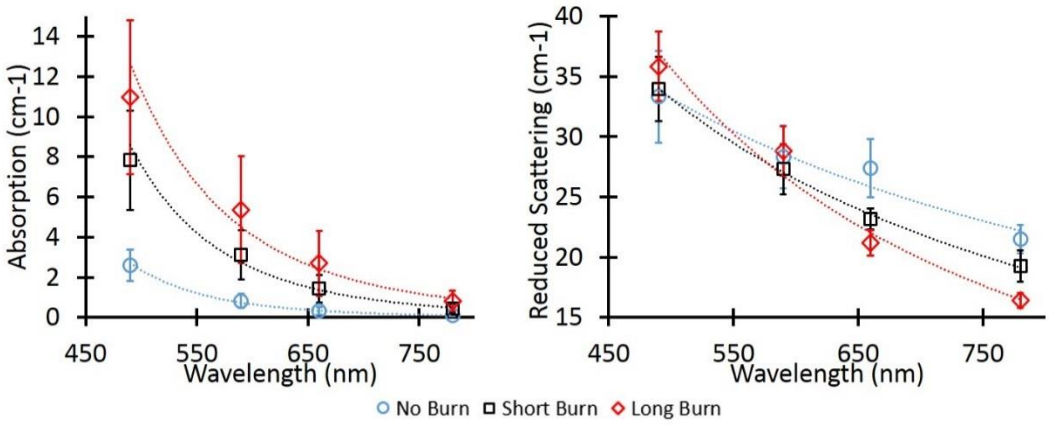


Figure 4.6. Optical properties for all samples. (a) shows the absorption as a function of wavelength for each burn duration. (b) shows the reduced scattering as a function of wavelength for each burn duration. Error bars are the standard deviation for all samples.

We then obtained the maps of the scattering parameter A and b by using the multi-wavelength information. (Figure 4.7a) and (Figure 4.7b) show the maps of A and b for the same sample shown in (Figure 4.5). Due to the large difference in depth of penetration (and therefore interrogation volume), the 490nm measurement was excluded from the multi-wavelength analysis. As (Figure 4.8a) indicates, the scattering parameter b correlated very well with the burn depth measured by histological analysis for all samples. The results indicate that the deeper the burn the higher the value of the b parameter. Additionally, as (Figure 4.8b) indicates, scattering power parameter was sufficient to fully characterize (100% sensitivity, 100% specificity) the burn severity characterized by the burn depth.

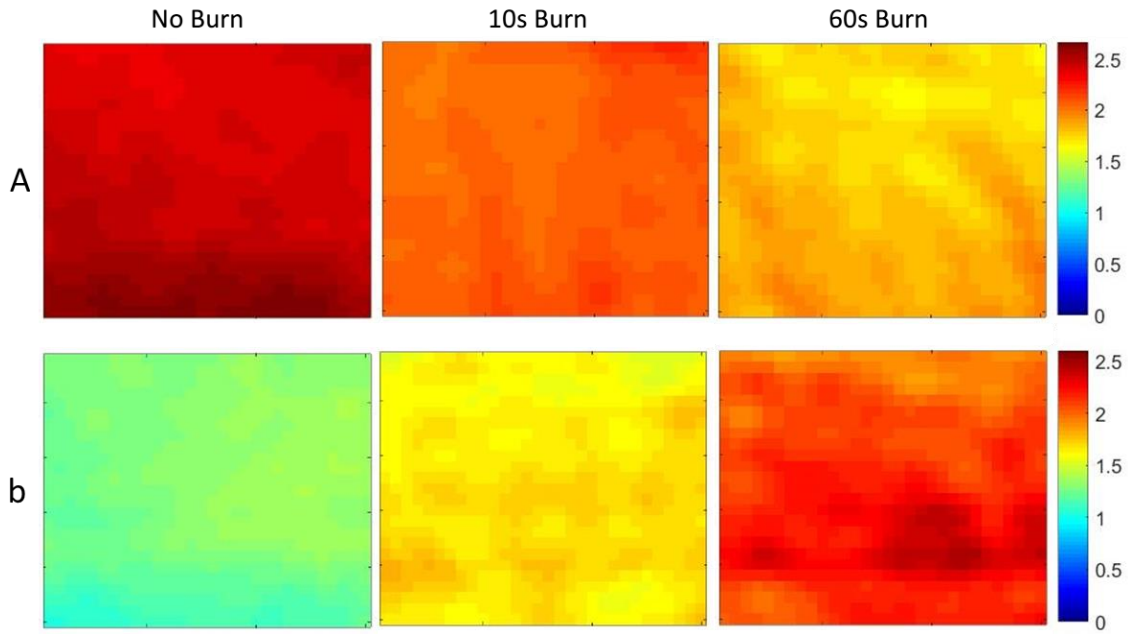


Figure 4.7. Multi-wavelength fitting results for scattering parameters A and b for one sample.

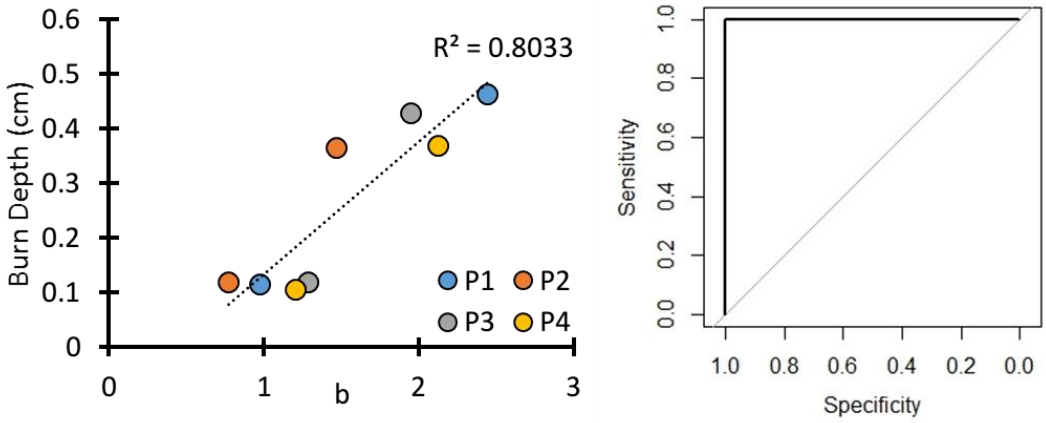


Figure 4.8. (a) Correlation with burn depth vs scattering power parameter b for each subject. (b) Sensitivity-specificity plot indicating full discrimination can be obtained by using this scattering parameter.

## 4.4 Discussion

Thermal injury is a clinically important problem associated with considerable morbidity and even mortality [3]. One important problem in this field is the need for the clinician to rapidly discern the burn severity, as a deeper burn would necessitate more aggressive treatment including fluid resuscitation and skin grafting [1], [3], [5]. We built a fast, clinic-friendly SFDI system to test whether this methodology could have use for early assessment of burns. The advantages of this system include that it is non-invasive, and can rapidly assess thermal burn injury severities [12], [13], [64], [78]. This technology could also be adapted to a hand-held instrument that would allow easy use in the field.

In this study, the measurements were taken from *ex vivo* tissue so hemoglobin absorption is expected to contribute little to the overall tissue absorption. Therefore, we expect that most of the changes in optical contrast is due to scattering component, which is primarily related to changes in the cellular structure. Our results have shown an increase in scattering power (b), and a decrease in scattering amplitude (A). The decrease in b is related to the decreasing size of the cellular structure, while an increase in A is related to the increase in density. The changes in scattering parameters could be caused by the dehydration of the skin cells, which could lead to shrinkage and formation of a thick and compact layer of dead cells as seen in the histology sections (Figure 4.4). With increased burn duration, the thickness of this layer also increases. This may explain the increase in the scattering parameter b. As for the observed increase in scattering parameter A, it may be due the interrogation of a smaller volume as the layer of compact volume of dead cells becomes homogenous as compared to the healthy cells. As burn

severity increase, darker pigmentation could occur. The dark pigmentation would increase absorption parameter ($\mu_a$) with increasing burn duration as shown in (Figure 4.6), thereby would decrease photon penetration depth and the volume of cells interrogated. It should be noted that the pathophysiology of burn *in vivo* and *ex vivo* differs with respect to time. This is due to the circulation of blood and the activation of inflammatory response. Response such as hyperemia or the formation of blister is not evident in an *ex vivo* sample. Nevertheless, this study provides insights into the changes that occur in the scattering properties of a burn wound, which assist in the quantification of the structural changes in the burn wound.

Future directions include using a porcine burn model to obtain *in vivo* data [6], [32]. Burns *in vivo* will alter the vasculature and hemodynamic changes (such as THC and StO2) will provide an additional source of contrast for burn severity estimation [12], [13], [64], [78]. Nevertheless, the present pilot studies provide the first use of the SFDI technology to characterize thermal burn injury on human skin *ex vivo*. This simple model could be adapted for use in other environmental injuries to include caustic agents and vesicants.

## 4.5 Improvements for In vivo Studies

### 4.5.1 Multilayered Quantification of Optical Properties

Current methods in obtaining the tissue optical properties are often based on the diffusion approximation that is derived from the photon transport equation [42], [59], [60], [62], [66], [79]–[81]. However, this approximation assumed a spatially homogenous turbid media, which is not the case for most biological samples. In fact, biological sample contains multiple layers and in the case of skin, at least three distinct layers (Figure 2.1) [17], [27], [62]. This assumption may result in a loss of important physiological information from the layers. Using a Monte Carlo photon propagation stimulation, a top layer with high absorption is added to stimulate the boundary between the epidermis and the dermis (Figure 4.) using a freely available code provided by Wang et al. [80]. This stimulation shows the vast differences between a homogenous and a two-layer model, where most of the photons are diffused within the top layer.

Although the multilayered equation has been derived and used by multiple groups, it is usually based on a single point source and therefore only applicable in the axial and not the transverse direction [42], [60], [75], [81]–[84]. By expanding the point sources of the diffuse photon density waves (DPDW) into a spatially modulated plane, Weber et al. has adapted the equation for a planar photon density wave (PPDW) model for multilayered turbid media [62]. However, to extract the optical properties of each layer, this model will have to fit the diffuse reflectance with five parameters (Figure 4.). These parameters are the absorption and reduced scattering for each layer ($\mu_{a1}$, $\mu_{s1}$', $\mu_{a2}$,

$\mu_{s2}$') and the top layer thickness, d, so that we can represent the modeled and measured reflectance with the five parameters as $R_d(\mu_{a1}, \mu'_{s1}, \mu_{a2}, \mu'_{s2}, d)$.

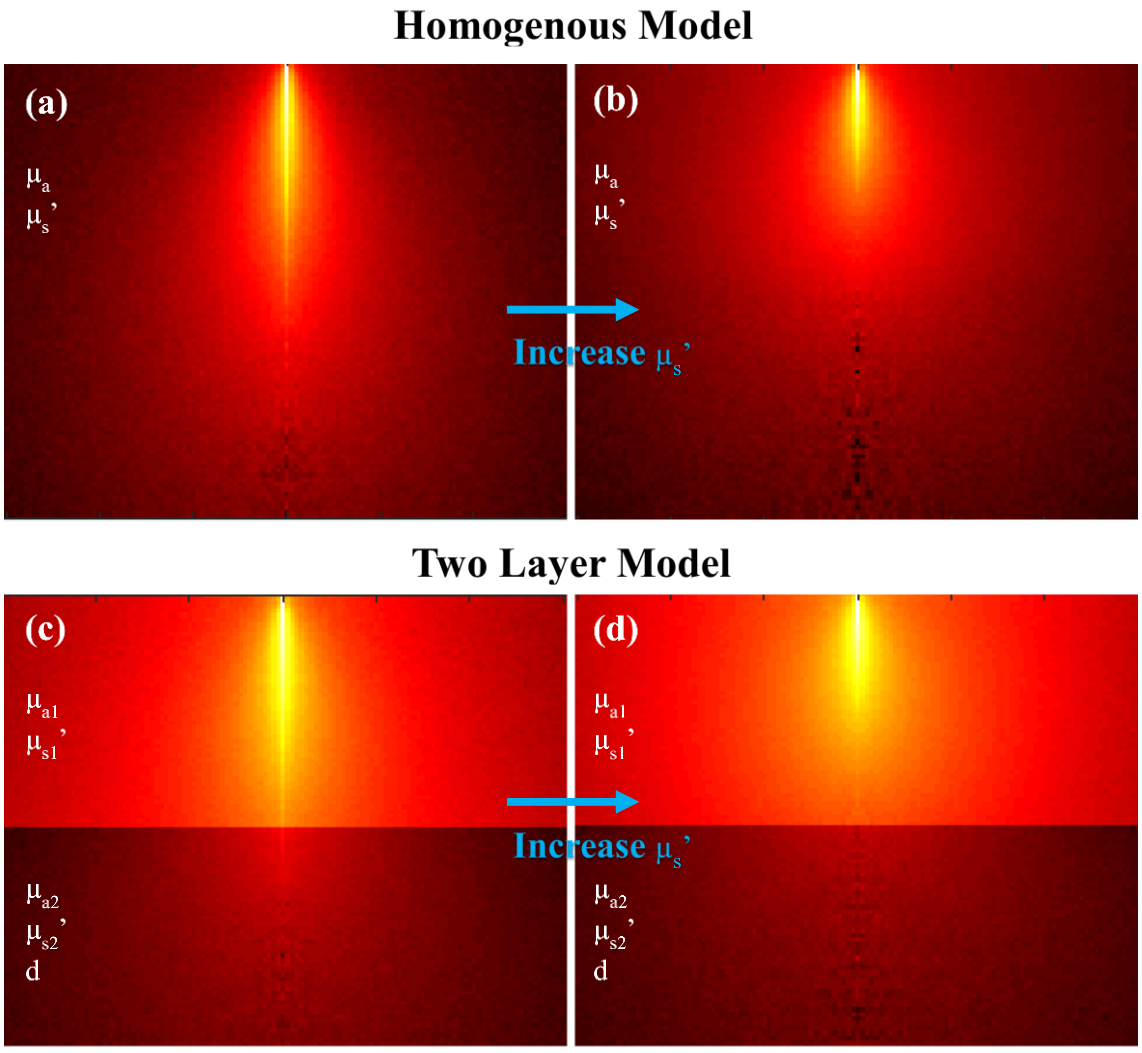


Figure 4.9. Monte Carlo Stimulation of photon diffusion in a homogenous medium and a two-layer medium. The two-layer model is more representative of biological systems such as the skin. A top layer with high $\mu_a$ is added to stimulate the epidermal and dermal layers of the skin. The increasing $\mu_s$' is to stimulate the physiological changes due to increased burn duration as shown previously. However, this model introduces three more variables to be quantified and measured.

### 4.5.2 Combined Ultrasound and SFDI to Improve Accuracy

Since three additional unknowns are introduced to model the layered skin tissue, using a homogenous model would inaccurately quantify the tissue optical properties. This problem becomes increasingly evident as more layers are added, but here in our research we mainly focus on the two-layer approximation as a first-stage improvement. Weber et al. has also shown that the fitting with five unknowns can create unstable fit results with respect to given initial conditions and the quantified parameters can deviate from the expected ones by more than 50% [62]. To overcome this problem, we propose the use high frequency ultrasound (HFUS) to reduce the unknowns, by obtaining the layer thickness of the sample. In addition to this information, a lower wavelength and high spatial frequency (Fx) can be chosen to approximate the penetration depth to superficial layers, so that the optical properties of the top layer can be resolved first and then these parameters can be used in subsequent fitting for the second layer optical properties quantification, as shown in (Figure 4.10).

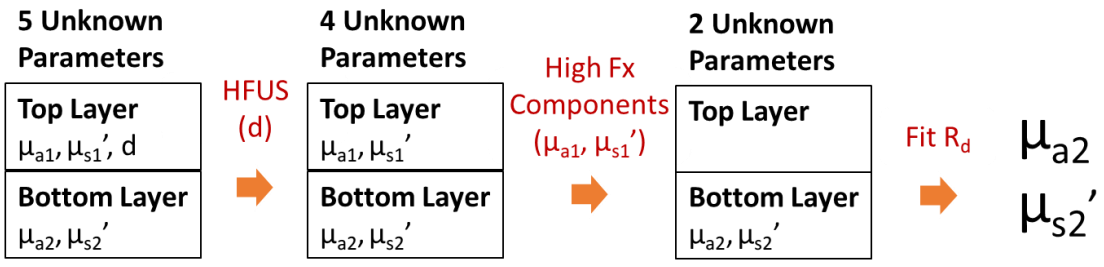


Figure 4.10. Extracting optical properties from the bottom layer by reducing unknown parameters in a two-layer PPDW.

### 4.5.3 Experimental Approach

To test this approach, a skin-liked phantom will be constructed. A top layer of approximately 0.15mm will be made with a high absorption and scattering coefficients using India ink and titanium dioxide respectively to stimulate burn on the epidermis [27], [73]. The layer will be made with PDMS and overlaid above a phantom with known properties. This layer will be examined with a HFUS (20MHz) setup that we have already built and tested (Figure 4.11).

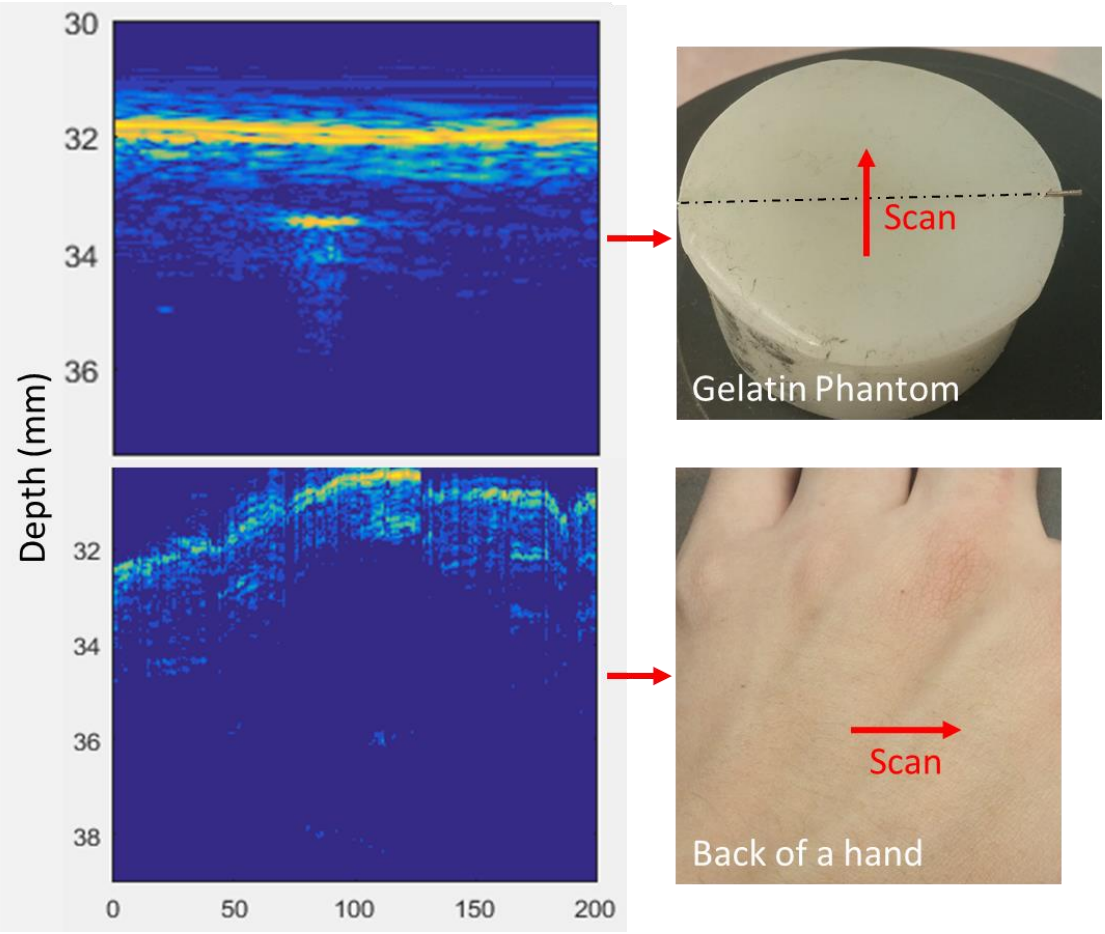


Figure 4.11. High Frequency Ultrasound was used on a gelatin phantom that has a metal wire inserted 1mm beneath the surface. It was also used on the back of a hand to visualize the layers in the skin. The scan was performed with B-Mode and traverse with a stepper motor at a transverse resolution of 100um.

To obtain the optical properties of the top layer in the two-layer phantom, the depth information obtained from HFUS can be used to estimate the penetration depth and therefore predict the spatial frequencies (Eqn (3.5)) that should be used (Figure 4.12).

With this approach, we hypothesize that the fitting error would be reduced and thus increasing the accuracy of the quantified optical properties for both layers and that it would have a higher accuracy compared to the homogenous model. This would be expected, as the three additional "unknowns" introduced with the two-layer model are reduced to two and so stabilizing the optical properties of the second layer.

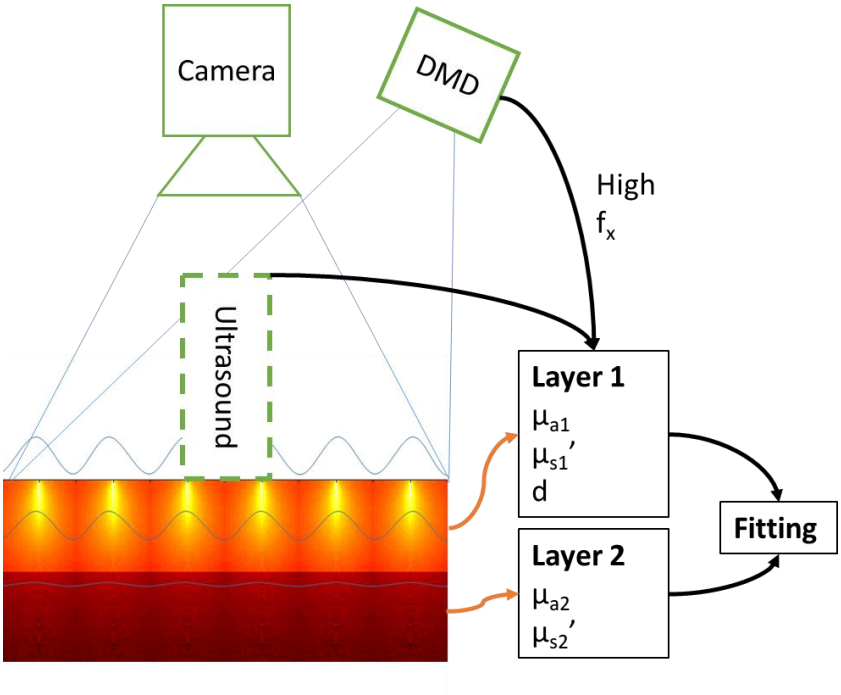


Figure 4.12. Proposed setup of the two-layer phantom study. The high spatial frequencies will be used to quantify $\mu_{a1}$ and $\mu_{s1}$' while HFUS will be used to obtain the layer thickness, d. The data will then be used to fit for the second layer.

# CHAPTER 5: FUTURE DIRECTIONS

Our goal is to perform this study on an *in vivo* model that closely imitates the physiology of humans, such as a porcine model [6], [12], [32], [78]. Since, this model would include blood parameters, the simple scattering parameter model that is derived from the previous study (Figure 4.8) could be combined with further analysis on the hemoglobin parameters – blood saturation and total hemoglobin concentration – to further improve the accuracy.

Ideally, the porcine model would be anesthetize and burnt with a metal block with increasing burn duration (Figure 5.1). This is to stimulate different burn grades with ample resolution within each grade so that the burn severity could be accurately distinguished. The imaging process would be similar to the phantom experiment described previously (Figure 4.12). The porcine model would also include wound healing, blood flow and inflammation, which are not accounted for in the previous study (Section 4.1), which the simple burn model may help to correct (Figure 4.8). We will test the two-layer model as an improvement of the homogeneous model and compare the results with the histopathology.

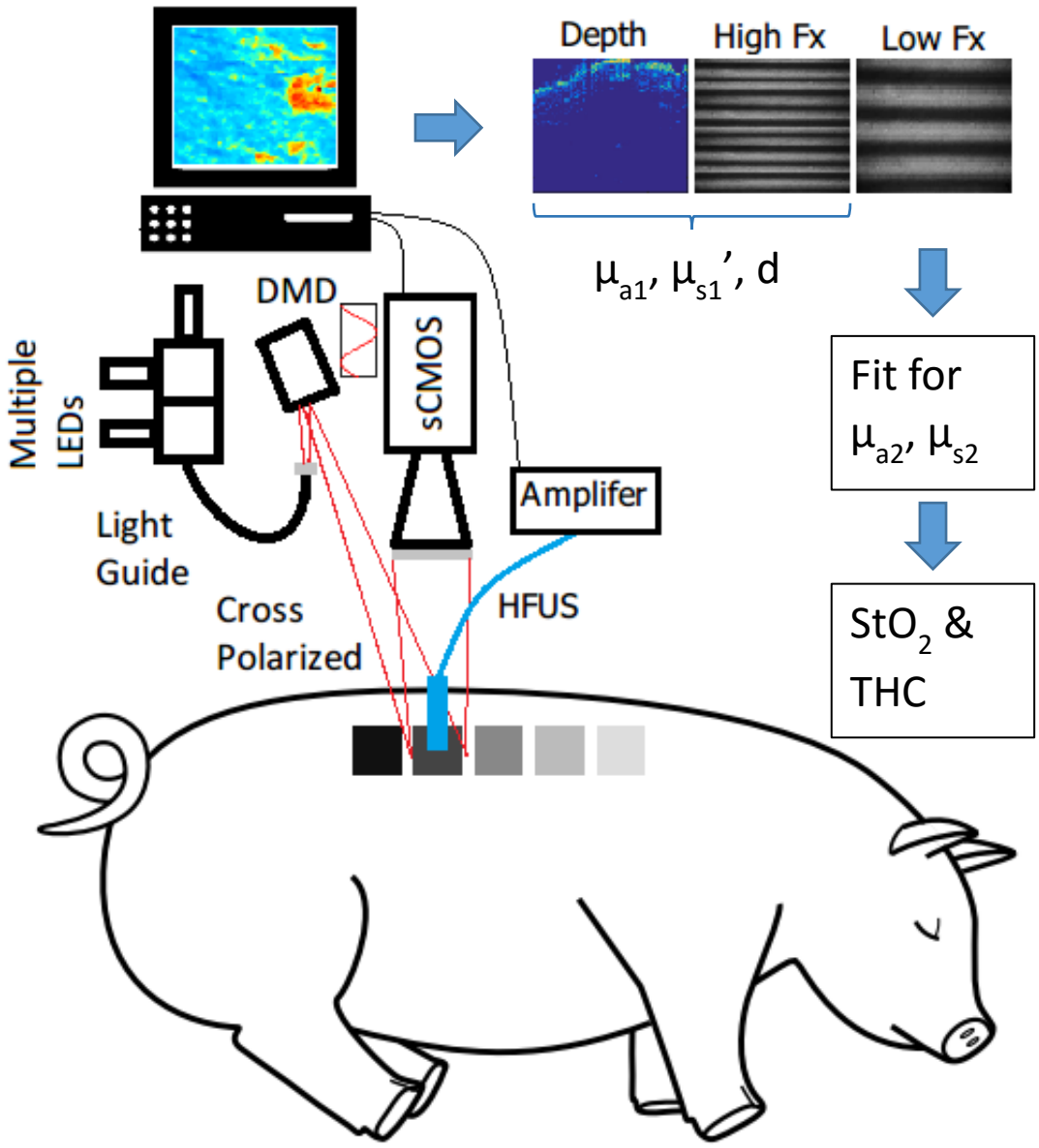


Figure 5.1. Proposed experimental setup for investigating burn wound in a porcine model with multi-wavelength and two-layered model SFDI, where it is burn for different durations to create different burn grades. The depth information is retrieved with HFUS and the optical properties for the top layer of skin are obtained with SFDI projecting high spatial frequencies. Using low spatial frequencies, the second layer can be quantified accurately with prior information. Finally, the oxygen saturation and hemoglobin concentration can also be quantified.

In summary, we hypothesize that these parameters would benefit from a two-layer model, due to an increased accuracy in estimating the optical properties, which will also

improve the quantification of the function contrast and ultimately the burn depth resolution.

# Bibliography


[1] S. Bhattacharya and R. K. Mishra, “Burn wound: How it differs from other wounds?,” *Indian J Plast Surg*, vol. 45, no. 2, pp. 364–373, 2012.

[2] S. Monstrey, H. Hoeksema, J. Verbelen, A. Pirayesh, and P. Blondeel, “Assessment of burn depth and burn wound healing potential,” *Burns*, vol. 34, no. 6, pp. 761–769, 2008.

[3] S. F. Miller, P. Bessey, C. W. Lentz, J. C. Jeng, M. Schurr, and S. Browning, “National Burn Repository 2007 Report: A Synopsis of the 2007 Call for Data,” *J. Burn Care Res.*, vol. 29, no. 6, pp. 862–870, 2008.

[4] Hylton J.G. Haynes, “Fire loss in the United States during 2014,” *Nfpa*, vol. 9/15, no. September, pp. 7–12, 2015.

[5] E. M. Renz and L. C. Cancio, “Acute Burn Care,” in *Combat Casualty Care: Lessons Learned from OEF and OIF*, E. Savitsky and B. Eastridge, Eds. Office of the Surgeon General, Borden Institute, 2012, pp. 593–639.

[6] A. J. Singer and S. A. McClain, “A Porcine Burn Model.,” in *Wound Healing: Methods and Protocols*, L. A. DiPietro and A. L. Burns, Eds. Totowa, NJ: Humana Press, 2003, pp. 107–190.

[7] A. M. Kahn, V. L. McCrady, and V. J. Rosen, “Burn wound biopsy. Multiple uses in patient management,” *Scand. J. Plast. Reconstr. Surg.*, vol. 13, no. 1, pp. 53–56, 1979.

[8] A. D. Jaskille, J. W. Shupp, M. H. Jordan, and J. C. Jeng, “Critical Review of Burn Depth Assessment Techniques: Part I. Historical Review,” *J. Burn Care Res.*, vol. 30, no. 6, pp. 937–947, 2009.

[9] D. Heimbach, L. Engrav, B. Grube, and J. Marvin, “Burn depth: A review,” *World J. Surg.*, vol. 16, no. 1, pp. 10–15, 1992.

[10] D. J. Cuccia, F. Bevilacqua, A. J. Durkin, F. R. Ayers, and B. J. Tromberg, “Quantitation and mapping of tissue optical properties using modulated imaging,” *J Biomed Opt*, vol. 14, no. 2, p. 24012, 2009.

[11] D. J. Cuccia, F. Bevilacqua, A. J. Durkin, and B. J. Tromberg, “Modulated imaging: quantitative analysis and tomography of turbid media in the spatial-frequency domain,” *Opt. Lett.*, vol. 30, no. 11, pp. 1354–1356, 2005.

[12] A. Mazhar, S. Saggese, A. C. Pollins, N. L. Cardwell, L. Nanney, and D. J. Cuccia, “Noncontact imaging of burn depth and extent in a porcine model using spatial frequency domain imaging,” *J Biomed Opt*, vol. 19, no. 8, 2014.

[13] J. Q. Nguyen, C. Crouzet, T. Mai, K. Riola, D. Uchitel, L.-H. Liaw, N. Bernal, A. Ponticorvo, B. Choi, and A. J. Durkin, “Spatial frequency domain imaging of burn wounds in a preclinical model of graded burn severity.,” *J. Biomed. Opt.*, vol. 18, no. 6, p. 66010, 2013.

[14] S. Gioux, A. Mazhar, B. T. Lee, S. J. Lin, A. M. Tobias, D. J. Cuccia, A. Stockdale, R. Oketokoun, Y. Ashitate, E. Kelly, M. Weinmann, N. J. Durr, L. a Moffitt, A. J. Durkin, B. J. Tromberg, and J. V Frangioni, “First-in-human pilot study of a spatial frequency domain oxygenation imaging system.,” *J. Biomed.*

*Opt.*, vol. 16, no. 8, p. 86015, 2011.

[15] D. J. Rohrbach, N. C. Zeitouni, D. Muffoletto, R. Saager, B. J. Tromberg, and U. Sunar, "Characterization of nonmelanoma skin cancer for light therapy using spatial frequency domain imaging," *Biomed. Opt. Express*, vol. 6, no. 5, p. 1761, 2015.

[16] D. J. Rohrbach, D. Muffoletto, J. Huihui, R. Saager, K. Keymel, A. Paquette, J. Morgan, N. Zeitouni, and U. Sunar, "Preoperative Mapping of Nonmelanoma Skin Cancer Using Spatial Frequency Domain and Ultrasound Imaging," *Acad. Radiol.*, vol. 21, no. 2, pp. 263–270, 2014.

[17] A. Bhandari, B. Hamre, O. Frette, K. Stamnes, and J. J. Stamnes, "Modeling optical properties of human skin using Mie theory for particles with different size distributions and refractive indices," *Opt Express*, vol. 19, no. 15, pp. 14549–14567, 2011.

[18] L. L. Chaikov, M. N. Kirichenko, S. V Krivokhizha, and A. R. Zaritskiy, "Dynamics of statistically confident particle sizes and concentrations in blood plasma obtained by the dynamic light scattering method," *J Biomed Opt*, vol. 20, no. 5, 2015.

[19] A. Lederer and H. J. Schope, "Easy-use and low-cost fiber-based two-color dynamic light-scattering apparatus," *Phys Rev E Stat Nonlin Soft Matter Phys*, vol. 85, no. 3 Pt 1, p. 31401, 2012.

[20] N. Bodenschatz, P. Krauter, S. Nothelfer, F. Foschum, F. Bergmann, A. Liemert, and A. Kienle, "Detecting structural information of scatterers using spatial

frequency domain imaging.," *J. Biomed. Opt.*, vol. 20, no. 11, p. 116006, 2015.

[21] J. M. Jensen and E. Proksch, "The skin's barrier.," *G. Ital. Dermatol. Venereol.*, vol. 144, no. 6, pp. 689–700, 2009.

[22] J. G. M. Jr. and J. J. M. Dermatologist, *Lookingbill and Marks' Principles of Dermatology*, 4e ed. 2013.

[23] "Human Skin Layers Diagram," *HealthFavo.Com*, 2013. [Online]. Available: http://healthfavo.com/wp-content/uploads/2013/09/labeled-skin-diagrams.gif.

[24] C.-H. Lee, M.-S. Kim, B. M. Chung, D. J. Leahy, and P. A. Coulombe, "Structural basis for heteromeric assembly and perinuclear organization of keratin filaments.," *Nat. Struct. Mol. Biol.*, vol. 19, no. 7, pp. 707–15, 2012.

[25] M. Haggstrom, "Layers of the epidermis," *Wikipedia*. [Online]. Available: https://en.wikipedia.org/wiki/Stratum_corneum#/media/File:Epidermal_layers.png .

[26] L. Eckhart, S. Lippens, E. Tschachler, and W. Declercq, "Cell death by cornification," *Biochim. Biophys. Acta - Mol. Cell Res.*, vol. 1833, no. 12, pp. 3471–3480, 2013.

[27] R. B. Saager, C. Kondru, K. Au, K. Sry, F. Ayers, and A. J. Durkin, "Multilayer silicone phantoms for the evaluation of quantitative optical techniques in skin imaging," *Proc. SPIE*, vol. 7567, pp. 756706-756706–8, 2010.

[28] D. Hutchinson, V. Ho, M. Dodd, H. N. Dawson, A. C. Zumwalt, and C. A. Colton, "Using Optical Coherence Tomography to Evaluate Skin Sun Damage and

Precancer," *Lasers Surg Med.*, vol. 148, no. 4, pp. 825–832, 2008.

[29] D. M. G. Jackson, "The diagnosis of the depth of burning," *Br. J. Surg.*, vol. 40, no. 164, pp. 588–596, 1953.

[30] R. B. O. William D James, Timothy G Berger, Dirk M Elston, *Andrews' Diseases of the Skin: clinical Dermatology. Saunders Elsevier*, 10e ed., vol. 33. Saunders, 2006.

[31] J. A. Marx, R. S. Hockberger, R. M. Walls, J. Adams, and P. Rosen, *Rosen's emergency medicine : concepts and clinical practice*, vol. 14. 2006.

[32] T. P. Sullivan, W. H. Eaglstein, S. C. Davis, and P. Mertz, "The pig as a model for human wound healing.," *Wound repair Regen.*, vol. 9, no. 2, pp. 66–76, 2001.

[33] "Different Burn Depth Characteristics," *The Victorian Adult Burns Service, Alfred Health, Melbourne, Australia*, 2012. [Online]. Available: https://www.vicburns.org.au/burns-assessment/burn-depth/different-burn-depth-characteristics.html. [Accessed: 01-Jan-2016].

[34] W. J. Mileski, L. Atiles, G. Purdue, R. Kagan, J. R. Saffle, D. N. Herndon, D. Heimbach, a Luterman, R. Yurt, C. Goodwin, and J. L. Hunt, "Serial measurements increase the accuracy of laser Doppler assessment of burn wounds.," *J. Burn Care Rehabil.*, vol. 24, no. 4, pp. 187–91, 2003.

[35] A. D. Kim and A. Ishimaru, "Optical diffusion of continuous-wave, pulsed, and density waves in scattering media and comparisons with radiative transfer.," *Appl. Opt.*, vol. 37, no. 22, pp. 5313–5319, 1998.

[36] D. Contini, F. Martelli, G. Zaccanti, A. Taddeucci, D. Contini, A. Taddeucci, and G. Zaccanti, “Photon migration through a turbid slab described by a model based on diffusion approximation. I. Theory.,” *Appl. Opt.*, vol. 36, no. 19, pp. 4587–99, 1997.

[37] T. Durduran, A. G. Yodh, B. Chance, and D. A. Boas, “Does the photon-diffusion coefficient depend on absorption?,” *J Opt Soc Am A Opt Image Sci Vis*, vol. 14, no. 12, pp. 3358–3365, 1997.

[38] J. Senarathna, A. Rege, N. Li, and N. V. Thakor, “Laser speckle contrast imaging: Theory, instrumentation and applications,” *IEEE Rev. Biomed. Eng.*, vol. 6, 2013.

[39] L. Spinelli, M. Botwicz, N. Zolek, M. Kacprzak, D. Milej, P. Sawosz, A. Liebert, U. Weigel, T. Durduran, F. Foschum, A. Kienle, F. Baribeau, S. Leclair, J.-P. Bouchard, I. Noiseux, P. Gallant, O. Mermut, A. Farina, A. Pifferi, A. Torricelli, R. Cubeddu, H.-C. H.-C. Ho, M. Mazurenka, H. Wabnitz, K. Klauenberg, O. Bodnar, C. Elster, M. Bénazech-Lavoué, Y. Bérubé-Lauzière, F. Lesage, D. Khoptyar, a. a. Subash, S. Andersson-Engels, P. Di Ninni, F. Martelli, and G. Zaccanti, “Determination of reference values for optical properties of liquid phantoms based on Intralipid and India ink,” *Biomed. Opt. Express*, vol. 5, no. 7, 2014.

[40] U. Sunar, H. Quon, T. Durduran, J. Zhang, J. Du, C. Zhou, G. Yu, R. Choe, A. Kilger, R. Lustig, L. Loevner, S. Nioka, B. Chance, and A. G. Yodh, “Noninvasive diffuse optical measurement of blood flow and blood oxygenation for monitoring radiation therapy in patients with head and neck tumors: a pilot study,” *J. Biomed.*

*Opt.*, vol. 11, no. 6, 2006.

[41] T. L. Troy and S. N. Thennadil, "Optical properties of human skin in the near infrared wavelength range of 1000 to 2200 nm," *J Biomed Opt*, vol. 6, no. 2, pp. 167–176, 2001.

[42] J. Ripoll, J. P. Culver, D. N. Pattanayak, A. G. Yodh, and M. Nieto-vesperinas, "Recovery of optical parameters in multiple-layered diffusive media: theory and experiments," *J. Opt. Soc. Am. A Opt. Image Sci. Vis.*, vol. 18, no. 4, pp. 821–30, 2001.

[43] T. Lister, P. A. Wright, and P. H. Chappell, "Optical properties of human skin," *J Biomed Opt*, vol. 17, no. 9, p. 90901, 2012.

[44] S. L. Jacques, "Optical properties of biological tissues: a review," *Phys. Med. Biol.*, vol. 58, no. 14, pp. 5007–5008, 2013.

[45] J. R. Mourant, T. Fuselier, J. Boyer, T. M. Johnson, and I. J. Bigio, "Predictions and measurements of scattering and absorption over broad wavelength ranges in tissue phantoms," *Appl. Opt.*, vol. 36, no. 4, p. 949, 1997.

[46] S. L. Jacques, "Optical assessment of cutaneous blood volume depends on the vessel size distribution : a computer simulation study," *J Biophotonics*, vol. i, no. 1, pp. 75–81, 2010.

[47] M. Xu, W. Cai, M. Lax, and R. R. Alfano, "Photon-transport forward model for imaging in turbid media.," *Opt. Lett.*, vol. 26, no. 14, pp. 1066–1068, 2001.

[48] S. L. Jacques and B. W. Pogue, "Tutorial on diffuse light transport," *J Biomed*

*Opt*, vol. 13, no. 4, 2008.

[49] K. M. Yoo, F. Liu, and R. R. Alfano, "When does the diffusion approximation fail to describe photon transport in random media?," *Phys. Rev. Lett.*, vol. 64, no. 22, pp. 2647–2650, 1990.

[50] M. C. W. van Rossum and T. M. Nieuwenhuizen, "Multiple scattering of classical waves: from microscopy to mesoscopy and diffusion," *Rev. Mod. Phys.*, vol. 71, no. 1, p. 86, 1998.

[51] L. V Wang and S. L. Jacques, "Source of error in calculation of optical diffuse reflectance from turbid media using diffusion theory.," *Comput. Methods Programs Biomed.*, vol. 61, no. 3, pp. 163–170, 2000.

[52] K. Lee, "Optical mammography: Diffuse optical imaging of breast cancer," *World J Clin Oncol*, vol. 2, no. 1, pp. 64–72, 2011.

[53] D. A. Boas, "Diffuse photon probes of structural and dynamical properties of turbid media: Theory and biomedical application," p. 260, 1996.

[54] J. Ripoll, R. B. Schulz, and V. Ntziachristos, "Free-space propagation of diffuse light: theory and experiments.," *Phys. Rev. Lett.*, vol. 91, no. 10, p. 103901, 2003.

[55] H. Wabnitz, D. R. Taubert, M. Mazurenka, O. Steinkellner, A. Jelzow, R. Macdonald, D. Milej, P. Sawosz, M. Kacprzak, A. Liebert, R. Cooper, J. Hebden, A. Pifferi, A. Farina, I. Bargigia, D. Contini, M. Caffini, L. Zucchelli, L. Spinelli, R. Cubeddu, and A. Torricelli, "Performance assessment of time-domain optical brain imagers, part 1: basic instrumental performance protocol," *J Biomed Opt*,

vol. 19, no. 8, p. 86010, 2014.

[56] K. Verdecchia, M. Diop, T. Y. Lee, and K. St Lawrence, “Quantifying the cerebral metabolic rate of oxygen by combining diffuse correlation spectroscopy and time-resolved near-infrared spectroscopy,” *J Biomed Opt*, vol. 18, no. 2, 2013.

[57] A. D. Mora, D. Contini, S. Arridge, F. Martelli, A. Tosi, G. Boso, A. Farina, T. Durduran, E. Martinenghi, A. Torricelli, and A. Pifferi, “Towards next-generation time-domain diffuse optics for extreme depth penetration and sensitivity,” *Biomed Opt Express*, vol. 6, no. 5, pp. 1749–1760, 2015.

[58] A. K. Dunn, C. L. Smithpeter, A. J. Welch, and R. R. Richards-Kortum, “Finite-difference time-domain simulation of light scattering from single cells,” *J Biomed Opt*, vol. 2, no. 3, pp. 262–266, 1997.

[59] T. H. Pham, T. Spott, L. O. Svaasand, and B. J. Tromberg, “Quantifying the properties of two-layer turbid media with frequency-domain diffuse reflectance.,” *Appl. Opt.*, vol. 39, no. 25, pp. 4733–45, 2000.

[60] A. Kienle, M. S. Patterson, N. Dognitz, R. Bays, G. Wagnieres, and H. van den Berg, “Noninvasive determination of the optical properties of two-layered turbid media,” *Appl. Opt.*, vol. 37, no. 4, pp. 779–791, 1998.

[61] S. L. Jacques, “Optical properties of biological tissues: a review,” *Phys Med Biol*, vol. 58, no. 11, pp. R37–R61, 2013.

[62] J. R. Weber, D. J. Cuccia, A. J. Durkin, and B. J. Tromberg, “Noncontact imaging of absorption and scattering in layered tissue using spatially modulated structured

light," *J. Appl. Phys.*, vol. 105, no. 10, pp. 1–9, 2009.

[63] A. Yafi, T. S. Vetter, T. Scholz, S. Patel, R. B. Saager, D. J. Cuccia, G. R. Evans, and A. J. Durkin, "Postoperative quantitative assessment of reconstructive tissue status in a cutaneous flap model using spatial frequency domain imaging.," *Plast. Reconstr. Surg.*, vol. 127, pp. 117–130, 2011.

[64] J. Q. Nguyen, R. B. Saager, D. J. Cuccia, K. M. Kelly, J. Jakowatz, D. Hsiang, and A. J. Durkin, "Effects of motion on optical properties in the spatial frequency domain.," *J. Biomed. Opt.*, vol. 16, no. 12, p. 126009, 2011.

[65] T. B. Rice, E. Kwan, C. K. Hayakawa, A. J. Durkin, B. Choi, and B. J. Tromberg, "Quantitative, depth-resolved determination of particle motion using multi-exposure, spatial frequency domain laser speckle imaging," *Biomed Opt Express*, vol. 4, no. 12, pp. 2880–2892, 2013.

[66] L. O. Svaasand, T. Spott, J. B. Fishkin, T. Pham, B. J. Tromberg, and M. W. Berns, "Reflectance measurements of layered media with diffuse photon-density waves: a potential tool for evaluating deep burns and subcutaneous lesions.," *Phys. Med. Biol.*, vol. 44, no. 3, pp. 801–13, 1999.

[67] A. Mazhar, D. J. Cuccia, T. B. Rice, S. A. Carp, A. J. Durkin, D. A. Boas, B. Choi, and B. J. Tromberg, "Laser speckle imaging in the spatial frequency domain," *Biomed Opt Express*, vol. 2, no. 6, pp. 1553–1563, 2011.

[68] N. Bodenschatz, A. Brandes, A. Liemert, and A. Kienle, "Sources of errors in spatial frequency domain imaging of scattering media.," *J. Biomed. Opt.*, vol. 19, no. 7, p. 71405, 2014.

[69] S. D. Konecky, A. Mazhar, D. Cuccia, A. J. Durkin, J. C. Schotland, and B. J. Tromberg, “Quantitative optical tomography of sub-surface heterogeneities using spatially modulated structured light.,” *Opt. Express*, vol. 17, no. 17, pp. 14780–90, 2009.

[70] M. Xu, Z. Cao, W. Lin, X. Chen, L. Zheng, and B. Zeng, “Single Snapshot Multiple Frequency Demodulation Technique for Spatial Frequency Domain Imaging,” *Opt. Soc. Am.*, vol. 81, 2014.

[71] J. Vervandier and S. Gioux, “Single snapshot imaging of optical properties.,” *Biomed. Opt. Express*, vol. 4, no. 12, pp. 2938–44, 2013.

[72] P. Diep, S. Pannem, J. Sweer, J. Lo, M. Snyder, G. Stueber, Y. Zhao, S. Tabassum, R. Istfan, J. Wu, S. Erramilli, and D. Roblyer, “Three-dimensional printed optical phantoms with customized absorption and scattering properties,” *Biomed Opt Express*, vol. 6, no. 11, pp. 4212–4220, 2015.

[73] F. Ayers, A. Grant, D. Kuo, D. J. Cuccia, and A. J. Durkin, “Fabrication and characterization of silicone-based tissue phantoms with tunable optical properties in the visible and near infrared domain,” *Proc. SPIE*, vol. 6870, pp. 7-1-7–9, 2008.

[74] T. Moffitt, Y. C. Chen, and S. A. Prahl, “Preparation and characterization of polyurethane optical phantoms,” *J Biomed Opt*, vol. 11, no. 4, p. 41103, 2006.

[75] S. Del Bianco, F. Martelli, F. Cignini, G. Zaccanti, A. Pifferi, A. Torricelli, A. Bassi, P. Taroni, and R. Cubeddu, “Liquid phantom for investigating light propagation through layered diffusive media,” *Opt Express*, vol. 12, no. 10, pp. 2102–2111, 2004.

[76] P. Lai, X. Xu, and L. V Wang, “Dependence of optical scattering from Intralipid in gelatin-gel based tissue-mimicking phantoms on mixing temperature and time,” *J Biomed Opt*, vol. 19, no. 3, p. 35002, 2014.

[77] P. Di Ninni, F. Martelli, and G. Zaccanti, “Intralipid: towards a diffusive reference standard for optical tissue phantoms.,” *Phys. Med. Biol.*, vol. 56, no. 2, 2011.

[78] A. Ponticorvo, D. M. Burmeister, B. Yang, B. Choi, R. J. Christy, and A. J. Durkin, “Quantitative assessment of graded burn wounds in a porcine model using spatial frequency domain imaging (SFDI) and laser speckle imaging (LSI),” *Biomed. Opt. Express*, vol. 5, no. 10, p. 3467, 2014.

[79] S. E. Skipetrov and R. Maynard, “Dynamic multiple scattering of light in multilayer turbid media,” *Phys. Lett. Sect. A Gen. At. Solid State Phys.*, vol. 217, no. 2–3, pp. 181–185, 1996.

[80] L. V Wang, S. L. Jacques, and L. Zheng, “MCML - Monte Carlo modeling of light transport in multi-layered tissues,” *Comput. Methods Programs Biomed.*, vol. 47, no. 1995, pp. 131–146, 1995.

[81] J. Li, G. Dietsche, D. Iftime, S. E. Skipetrov, G. Maret, T. Elbert, B. Rockstroh, and T. Gisler, “Noninvasive detection of functional brain activity with near-infrared diffusing-wave spectroscopy,” *J. Biomed. Opt.*, vol. 10, no. 4, p. 44002, 2005.

[82] G. Alexandrakis, T. J. Farrell, and M. S. Patterson, “Accuracy of the diffusion approximation in determining the optical properties of a two-layer turbid medium.,” *Appl. Opt.*, vol. 37, no. 31, pp. 7401–7409, 1998.

[83] A. Liemert and A. Kienle, “Light diffusion in N-layered turbid media: steady-state domain.,” *J. Biomed. Opt.*, vol. 15, no. 2, p. 25003, 2015.

[84] K. Verdecchia, M. Diop, A. Lee, and K. St Lawrence, “Characterization of a hybrid diffuse correlation spectroscopy and time-resolved near-infrared spectroscopy system for real-time monitoring of cerebral blood flow and oxygenation,” *Adv. Biomed. Clin. Diagnostic Surg. Guid. Syst. Xiii*, vol. 9313, 2015.